CrossMark

Interaction of Sea Breeze and Deep Convection over the Northeastern Adriatic Coast: An Analysis of Sensitivity Experiments Using a High-Resolution Mesoscale Model

GABRIJELA KEHLER-POLJAK,[1] MAJA TELIŠMAN PRTENJAK,[1] MARKO KVAKIĆ,[2] KRISTINA ŠARIRI,[3] and ŽELJKO VEČENAJ[1]

Abstract—This study investigates the sensitivity of a high-resolution mesoscale atmospheric model in the model reproduction of thermally induced local wind (i.e., sea breezes, SB) on the development of deep convection (Cb). The three chosen cases are simulated by the Weather and Research Forecasting (WRF-ARW) model at three (nested) model domains, whereas the area of the interest is Istria (peninsula in the northeastern Adriatic). The sensitivity tests are accomplished by modifying (1) the model setup, (2) the model topography and (3) the sea surface temperature (SST) distribution. The first set of simulations (over the three 1.5-day periods during summer) is conducted by modifying the model setup, i.e., microphysics and the boundary layer parameterizations. The same events are simulated with the modified topography where the mountain heights in Istria are reduced to 30% of their initial height. The SST distribution has two representations in the model: a constant SST field from the ECMWF skin temperature analysis and a varying SST field, which is provided by hourly geostationary satellite data. A comprehensive set of numerical experiments is statistically analyzed through several different approaches (i.e., the standard statistical measures, the spectral method and the image moment analysis). The overall model evaluation of each model setup revealed certain advantages of one model setup over the others. The numerical tests with the modified topography showed the influence of reducing the mountains heights on the pre-thunderstorm characteristics due to: (1) decrease of sensible heat flux and mid-tropospheric moisture and (2) change of slope-SB wind system. They consequently affect the evolution and dimensions of SBs and the features of the thunderstorm itself: timing, location and intensity (weaker storm). The implementation of the varying SST field in the model have an impact on the characteristics and dynamics of the SB and finally on the accuracy of Cb evolution, duration and the intensity. SST variations emphasized the importance of the phase matching in both daytime cycles of SB and Cb due to their extremely strong nonlinear relationship.

1. Introduction

According to the definition by Thunis and Bornstein (1996), mesoscale phenomena have spatial dimensions between 0.2 and 200 km and have been usually reproduced by mesoscale models. However, because of the steady increase in computing power, a significant increase in the resolution of global and regional, both meteorological and climate models (e.g., Prein et al. 2016), have enabled forecasts of a large majority of mesoscale processes. Despite this continuous advancement in numerical model performances, the deep convection is a mesoscale phenomenon that is still simulated and forecasted without sufficient precision (e.g., Arakawa and Jung 2011; Güttler et al. 2015). Numerous recent studies have shown a large scattering of thunderstorm forecasts (in both research and operational model versions) and great uncertainty in time, space and intensity in simulated convective processes and convective precipitation (e.g., Weisman et al. 2008; Clark et al. 2010b; Mohan and Bhati 2011; Jury and Chiao 2013). The difficulties of storm prediction are still particularly noticeable over complex terrain (e.g., Teixeira et al. 2014; Güttler et al. 2015).

Some of the uncertainty/inaccuracy in models arises from the selection of model setup and a variety of scheme options (e.g., Gómez-Navarro et al. 2015). Each new version of the widely used Weather and Research Forecasting (WRF) model (Skamarock et al. 2008) offers new selecting options for different physical parameterizations. Thus, the optimal model setup for a particular event, region and period under

[1] Department of Geophysics, Faculty of Science, University of Zagreb, Zagreb, Croatia. E-mail: poljakica555@yahoo.com; telisman@gfz.hr
[2] INRA, UMR 1391 ISPA, Villenave d'Ornon, France.
[3] Croatian Metrology Institute, Zagreb, Croatia.

consideration is always arbitrary. Over the last 10 years (e.g., Clark et al. 2010a), numerous studies have been performed to estimate the sensitivity of one or more physical options (so called "mixed physics") on the WRF's output for different purposes. In these studies, the authors investigated the influence of a cumulus convective parameterization scheme (e.g., Mayor and Mesquita 2015), microphysics scheme (e.g., Weisman et al. 2008; Givati et al. 2012; Horvath and Vilibić 2014), radiation scheme (Kleczek et al. 2014), land-surface model (e.g., Mohan and Bhati 2011), and an atmospheric boundary layer (ABL) scheme-surface layer scheme (e.g., Weisman et al. 2008; Acs et al. 2014; Gómez-Navarro et al. 2015; Cohen et al. 2015; Milovac et al. 2016) to improve forecasts, air quality simulations (e.g., Žabkar et al. 2013) or examine wind energy resources (e.g., Menendez et al. 2014). These authors have proposed various combinations of optimal scheme setups which equally depended on the region (terrain) and analyzed phenomena. Unfortunately, although these authors observed some general characteristics of the used schemes, their results indicate no straightforward general recipe for the simulation of the stormy events. According to Clark et al. (2010b), the model setup should be checked for each area (at least) and for similar types of events, keeping in mind that these schemes interact in a non-linear manner.

In our case, the area of interest is the northern edge of the Adriatic (Fig. 1) , which belongs to a very active convective region, not only in the Mediterranean but in Europe as well (Meteorological Office 1962; van Delden 2001; Brooks et al. 2003; Feudale and Manzato 2014; Stanešić and Brewster 2015). A very complex portion of the northeastern (NE) Adriatic coast (Istria and islands in Fig. 1) and mountainous terrain are located in Croatia, where up to 50 days with thunder per year are usual (Penzar et al. 2001). Relatively recent studies by Mikuš et al. (2012) and Poljak et al. (2014) showed some peculiarities of the stormy days in this complex region in terms of synoptic and mesoscale conditions. Using lightning data, Mikuš et al. (2012) observed the highest frequency of stormy days during the warm portion of the year, i.e., in $\sim 60\%$ of all days. Convection usually occurred during non-gradient

pressure conditions (21%) and low-pressure formations (cyclones and troughs, 72%). On 82% of overall stormy days, prevailing wind regimes on a large scale were from the southwest (SW, 46%), northeast (NE, 18%) and northwest (NW, 18%).

During the summer months over Istria, the occurrence of daytime cumulonimbus (Cb) clouds is quite usual (Feudale et al. 2013; Petrova et al. 2014) with the simultaneous evolution of the sea breezes (SBs) on the Adriatic shores (Prtenjak 2003; Prtenjak et al. 2008; Babić et al. 2012). Still, Poljak et al. (2014) have found significantly less frequent SB–Cb interactions during synoptic SW warm-wet flow in the front portion of cyclones or troughs over the area. Numerical simulations in Poljak et al. (2014) also revealed that the origin and Cb cell locations were completely controlled by the main elongated convergence zone, which resulted from at least two opposing SB systems along the peninsula: from southeast and west coasts. Lower tropospheric moisture distributions (below 700 hPa), which were influenced by both horizontal low-level moisture convergence and upward moisture advection by the SB front, played a significant role as well. However, the certain discrepancies between the model and observations in the lifetime, intensity and location of these deep convection characteristics have been found.

Although rarely studied, water body dimensions and accompanied sea surface temperature (SST) can affect the intensity and evolution of both SB systems (e.g., Segal and Pielke 1985; Sweeney et al. 2014) and convection itself (e.g. Miglietta et al. 2011). Several studies (Segal and Pielke 1985; Franchito et al. 1998, 2008) showed the very low dependence of the SB to the SST, except when a moderate geostrophic wind was included (Segal and Pielke 1985). On the other hand, Tang (2012) and Sweeney et al. (2014) stressed that the effect of SST on the SB is stronger than previously thought, because the SST can disturb the turbulent processes within the marine ABL and thus directly affects local coastal horizontal gradients of temperature and pressure. Miglietta et al. (2011) analyzed the effect of the SST on Mediterranean cyclones in southeastern Italy and showed that the typical features for a tropical cyclone noticeably change with variations in the SST. Warmer (colder)
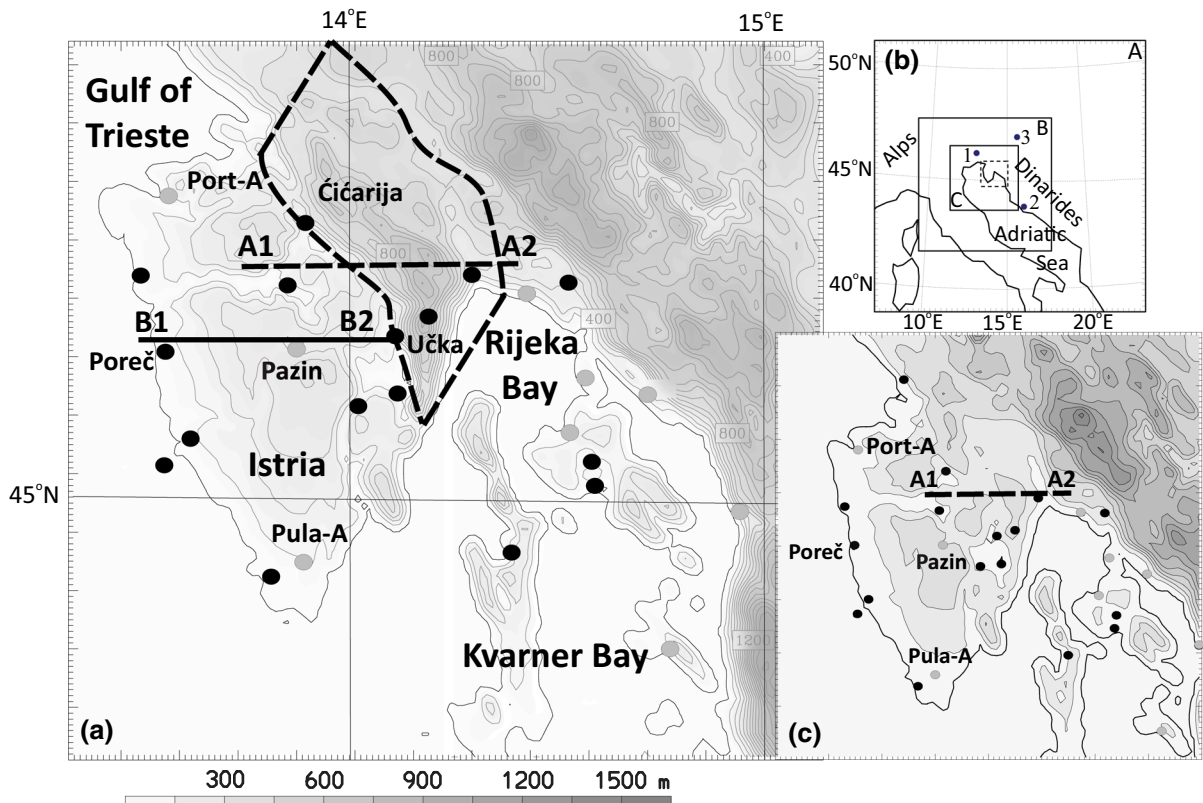
Figure 1

a Topographic map of the northeastern Adriatic coast (*dotted small rectangle* in **b**) with the positions of the measuring sites (*circles*); hourly meteorological measurements [*gray*; e.g., Pula Airport (*Pula-A*), Pazin and Portorož-Airport (*Port-A*)] and ordinary meteorological stations (*black*). Kvarner Bay encompasses the smaller Rijeka Bay and many islands. The *thick solid black line* denotes the base of vertical cross-section (*B1B2*) shown in later figures and Table 3. **b** The *upper right panel* indicates the coarse-grid (*A*), mid-frame (*B*) and fine-grid (*C*) WRF model domains, respectively. *Numbered dots 1* and *2* denote Udine (46.03°N, 13.18°E) and Zadar (44.10°N, 15.35°E) radiosounding stations, respectively. *Dot 3* shows the radar Lisca position (46.06°N, 15.28°E). **c** The *lower right panel* presents the modification of the topography used in the sensitivity test where the mountain massifs of Ćićarija (∼1100 m asl) and Učka (∼1400 m asl) were reduced to 30% of their initial height in the area marked by the *curved dashed* boundary in **a**. The cross-section (*A1A2*) shown in **a** and **c** is used to display the reduction in topography height (see Fig. 14 in Appendix 1)

SST produces stronger (weaker) sea-surface fluxes. This leads to the earlier (delayed) and enhanced (reduced) development of convection and the intensification of the cyclones. Both, SB (e.g., Crosman and Horel 2010) and Cb (e.g. Barthlott and Kirshbaum 2013) largely depend on the characteristics of nearby terrain, e.g., the slope and height of the coastal terrain, the coastline's curvature, location of the mountain relative to the coastline and atmospheric stability. Nevertheless, the results of the investigations that involve the effect of the SST on the development of the SB–Cb interactions over the northern Adriatic are still unknown. In addition,

divergences in the final conclusions regarding the effect of the SST on SBs in different regions suggest that these phenomena are not simply and unambiguously transferable (if at all) from one to the other locations. Thus may or may not confirm previous results from other areas.

Therefore, the main objectives of this study are as follows. (1) To evaluate the results of different WRF physics parameterization schemes versus measurements and find a model setup that satisfactorily simulates SB–Cb interaction. (2) To determine the sensitivity of the Istrian SB–Cb interplay to the coastal orography, which has not yet been performed.

(3) To explore the abilities of two various degrees of realistic SST fields in the WRF model and investigate the SST influence on SB–Cb interplay. (4) To compare the magnitude of deviations from mixed physics options and SST fields. This study follows up the work by Poljak et al. (2014) and thus complements and extends our knowledge about deep convection-local wind interplay. The results are also expected to improve the real-time forecast (especially weather forecasts for airports and aviation) of such daily recurrences in the area.

2. Data and Methodology

2.1. Area of Study and Data

The study area encompasses the NE Adriatic with a focus on the Istrian peninsula (Fig. 1). The western low coast rises slightly to the north and east of the peninsula, where the highest peaks, of Ćićarija and Učka Mountains are placed; ~ 1100 m (Ćićarija) and ~ 1400 m (Učka) above sea level (asl). Several stations with hourly measurements are located in Istria: the Portorož-Airport station (NW edge of the peninsula), the Pazin station (in the center of the peninsula) and the Pula-Airport station (near the tip of Istria). Eastward from the peninsula, the Kvarner Bay (consisting of the several larger and many smaller islands) contributes to the complexity of the NE Adriatic region. In this area, the semi-enclosed Adriatic Sea is shallow, with a maximum depth of 50 m, which suggests potential for large diurnal SST variations.

Majority available hourly observations such as 10-m wind, 2-m temperature and 2-m relative humidity (rh) are controlled and provided from the standard Croatian meteorological network (see positions in Fig. 1a). These measurements were obtained by the overall seven automated stations (10-min wind average and instantaneous T and rh) and 16 climatological stations (in three terms; 7, 14, 21 of local time). As the measurements were used from climatological stations, the wind speed measurements had to be converted from the Beaufort scale; therefore, the comparison with the model could be burdened by certain imprecision. In addition, METAR reports

from two additional airport sites every hour were also utilized, the Pula-Airport (Croatia, 44.9°N, 13.93°E, 63 m asl) and Portorož-Airport (Slovenia, 45.49°N, 13.6°E, 4 m asl; from https://www.wunderground.com/history/airport), as well as radiosoundings in Udine (Italy, 46.03°N, 13.18°E, 94 m asl) and Zadar (Croatia, 44.10°N, 15.35°E, 79 m asl; from http://weather.uwyo.edu/upperair/sounding.html). It is important to mention that the airport near-surface measurements from METAR reports for rh data can deviate from the real rh values by up to 5–10% because of the rounding of temperature values. Near-surface measurements were complemented by hourly radar images (i.e., radar reflectivity) from the Lisca radar station (Slovenia, 46.15°N, 15.38°E, 524 m asl; ARSO—http://www.meteo.si). All data were given in Coordinated Universal Time, UTC (Central European Time, CET = UTC + 1 h).

2.2. Chosen Cases

Three cases were selected for this study; case C1 (9 July 2006), C2 (8 August 2006) and C3 (8 June 2003) from database made by Babić et al. (2012). Each selected case contains interactions between SBs and Cb above Istria, which were quite extensively analyzed in Poljak et al. (2014). The main criterion for selection was done by observation of the noon/
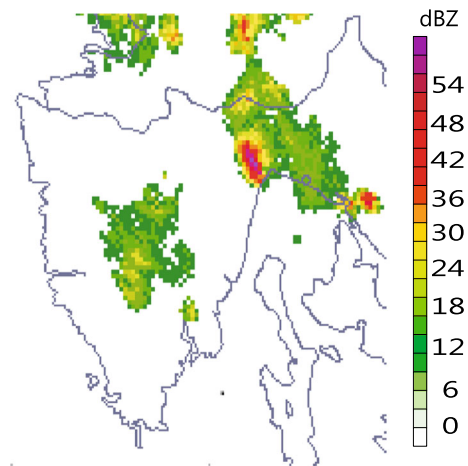

Figure 2
Measured radar reflectivity factor (dBZ) in radar images on 9 July 2006 at 13 UTC (14 CET). Source: ARSO—http://www.meteo.si. The radar reflectivity legend is provided with a 3-dBZ interval

afternoon convection on radar images over the Istria (Fig. 2) which also means that SB could form along coasts.

In cases C1 and C2, a quasi-non-gradient pressure field formed over Istria after cyclone movement towards the Pannonia Plain and Black Sea. These pressure patterns were formed on the rear side of the cyclones and were associated with NE (in C1) and NW (in C2) offshore large-scale winds aloft (according to the radiosounding data). Local circulations (i.e., SB) in the lowest atmosphere occurred over the western and southeastern coastlines (e.g., Fig. 3). In time, the elongated, eastward-moving convergence zone was generated by opposite SBs (see black dashed lines in Fig. 3). Offshore large-scale wind in the upper troposphere [contributing to an average rh (850–500 hPa) > 60%] and the convergence zone in the lowermost troposphere affected the lifetimes and movements of the initial Cbs. Over the Istrian mountain range, the formation of the first Cbs was noticeable. They were followed by the development of new CB cells along the convergence zone after merging of the SB fronts (SBF) and thunderstorm outflows.

The shortest and weakest thunderstorm event occurred in case C3 under the influence of the rear southern side of an anticyclone, with the support of a shallow elevated cyclone over Sardinia and diffluent flow over central Europe. This event was characterized by the highest low-level moisture, relatively unfavorable mid-tropospheric humidity and large-scale SE onshore wind (visible in the Zadar sounding, not shown). In this case, SB systems (western and southeastern) along the coast were also developed creating the convergence zone along the peninsula. Opposite to the C1 and C2 case (where the convection started over mountains), in C3 case the most important driving Cb mechanisms was humidity advection by the SBF, which elevated both, the amount and the depth of humidity in the mid-troposphere. In this case, the western SB was the predominant feature during the afternoon, when the generated deep convection was relatively weak and limited.

All three cases revealed some common local atmospheric conditions: (1) large-scale wind speeds (0–6 km) ≲ 10 m/s; (2) positive daytime low-level temperature differences between the land and sea (>1.5 °C); (3) the late-morning formation of a narrow convergence zone from western and southeastern SBs; (4) CAPE (up to 3 km) >500 J/kg, (5) an average mid-tropospheric rh (850–500 hPa) > 60% and/or high levels of low-level moisture; and (6) the maximum intensity of storms during the afternoon.

2.3. Model Setup and Numerical Experiments

We applied the nonhydrostatic WRF-ARW (WRF-Advanced Research version V3.6) model (Table 1). The WRF model solves the fully compressible, nonhydrostatic equations of motion in an Arakawa-C grid with the terrain following vertical coordinates. In the model, three model domains (Fig. 1) were chosen on a Lambert conformal projection and two-way nesting. Grid spacing configurations (and a number of grid points) were 13.5-km (79×79), 4.5-km (136×118) and 1.5-km (199×190), which supported an acceptable relationship between model ability to discern investigated phenomena and time of calculation. Although some impact on the domain size on the SB–CB interaction could exist, here this effect has not been tested. Eighty-one levels comprise the vertical grid, starting with the lowest half-sigma level at ~ 10 m above the ground, covering the lowermost 2 km with 13 levels and finishing at 50 hPa. We run simulations without nudging option at a cluster of HP ProLiant BL460c G1 servers with Intel(R) Xeon(R) CPU E5430@2.66 GHz processors. Number of CPUs used for running the simulation was up to 56. The output files contain fields every hour.

The control simulation uses a full suite of parameterization schemes, including a mixed-phase microphysics Pardue Lin scheme (Lin et al. 1983); an Eta surface layer parametrization that is based on the Monin–Obukhov theory and Mellor–Yamada–Janjić (MYJ) scheme for the ABL (Janjić 1994); a rapid radiative-transfer model scheme (Mlawer et al. 1997); a five-layer thermal diffusion scheme (Dudhia 1996) for soil temperature; and a Dudhia scheme (Dudhia 1989) for long-wave and short-wave radiation, respectively. Convective parameterization (Betts–Miller–Janjić scheme; Janjić 1994) was only
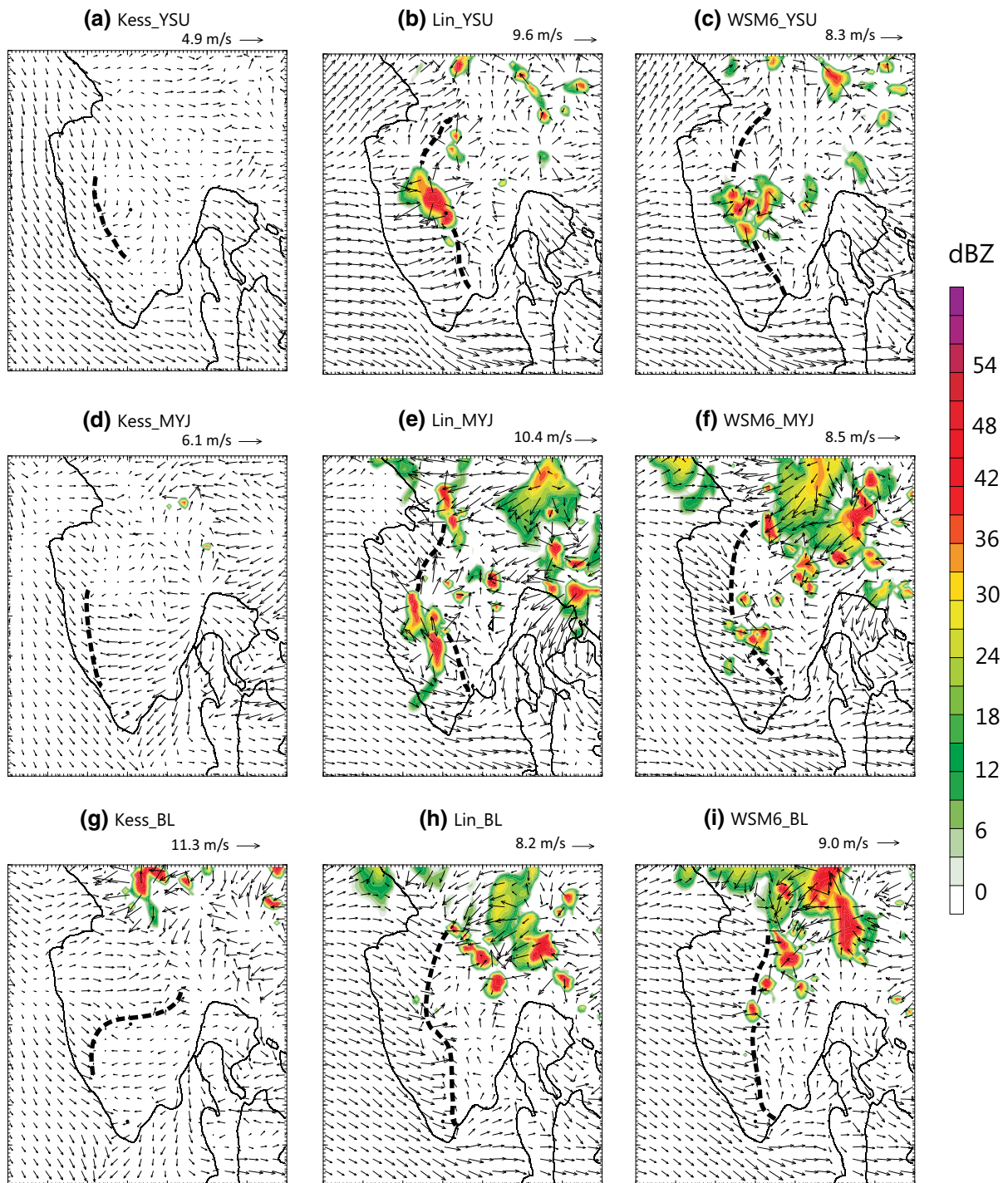
used in the two larger domains ($dx = 13.5$ and 4.5 km). Applying cumulus parameterization scheme (CPS), grid spacings in the range of 3–5 km represent a "gray zone" in which there is no clear recommendation whether to use parameterization or not (e.g., Gilland and Rowe 2012). Although we did not test the boundary, according to the results of other numerical studies (e.g., Žabkar

Modelled 10-m wind above ground level (in m/s) and the radar reflectivity factor (dBZ) for the numerical WRF tests in Table 1 on 9 July 2006 at 13 UTC (14 CET). Every third wind vector is drawn. The radar reflectivity legend is the same as in Fig. 2; provided with a 3-dBZ interval (*legend on the right*). Over peninsula, *dashed black lines* indicate the position of the main convergence zone in the wind fields. The shown maximum reference vectors are different for each subfigure. The *same images but without wind vectors* represent input data for the image moments analysis

et al. 2013; Teixeira et al. 2014; Horvath and Vilibić 2014; Milovac et al. 2016) we decided to keep the CPS at 4.5 km and deactivated it at 1.5 km resolution. The topography and land use in the model were derived from the U.S. Geological Survey's 24-category data set at a resolution of 30″, and data from the global ECMWF analysis were used as initial and boundary conditions every 6 h on a 0.25° × 0.25° grid. Simulations of C1–C3 cases lasted 36 h starting at noon of the previous day because of the spin-up time (here considered first 12 h). Skamarock and Klemp (2008) suggested that a minimum of 12 h spin-up time should be used to exclude the occurrence of instabilities in the mesoscale numerical model.

In order to identify differences in model performance, we defined 39 numerical experiments to seek an optimal model setup for SB–Cb interactions (Table 1). These numerical experiments with mixed physics comprised 13 combinations of microphysics, ABL and surface layer schemes per case. Every experiment was called by a combination of the "Microphysics_ABL" options (see Table 1).

The selection criteria for the ABL scheme were based on the differences between local and nonlocal approaches to ABL modelling. Therefore, the widely used local MYJ and nonlocal Yonsei University (YSU) (Hong et al. 2006) ABL schemes were used alongside appropriate surface layer schemes; a revised MM5 scheme was used for all the model runs with YSU and the Eta similarity scheme with the MYJ scheme. The YSU scheme explicitly treats the entrainment process by providing strong convective mixing in a convective situation, and less mixing for mechanically generated turbulence. The MYJ scheme is a 1.5-order closure scheme that is based on the concept of mixing length and equation for turbulence kinetic energy (TKE) prognosis. The third selected ABL scheme was Bougeault–Lacarrère (BouLac) scheme (Bougeault and Lacarrère 1989) and was run together with the Eta similarity scheme. The BouLac scheme is also a 1.5-order local closure scheme that includes a prognostic equation for TKE whose main objective is a better presentation of the transfer of momentum and heat in mountainous areas where gravity waves are one of the main factors in creating turbulence. The reason for its selection is the better performance of TKE in this scheme over the East Adriatic (Večenaj et al. 2012) during the analysis of strong wind.

Another design factor was the use of the microphysics schemes, which explicitly resolved water vapor, cloud, and precipitation processes. The options ranged from an excluded microphysics scheme (- marked by 0 in Table 1) and the very simple Kessler

Table 1

A list of numerical experiments containing the ABL and surface layer schemes, microphysics scheme, type of topography and source of SST field

Numerical experiments	Additional modifications		Microphysics scheme			
ABL and surface layer schemes	Topography	SST (source)	Disabled microphysics scheme	Kessler	Pardue Lin	WSM6
MYJ and Eta similarity	Original	ECMWF	0_MYJ	Kess_MYJ	Lin_ MYJ	WSM6_MYJ
	Original	MSG SEVIRI_1 h	/	/	Lin_MYJ_SST	/
	Modified	ECMWF	/	/	Lin_MYJ_MT	/
YSU and revised MM5	Original	ECMWF	0_YSU	Kess_YSU	Lin_YSU	WSM6_YSU
BouLac and Eta similarity	Original	ECMWF	0_BL	Kess_ BL	Lin_BL	WSM6_BL

Every experiment is called as a combination of the "Microphysics_ABL" options

MSG Meteosat Second Generation, *SEVIRI* Spinning Enhanced Visible and Infrared Imager, *BL* BouLac ABL scheme

scheme (Kessler 1995) to more sophisticated and realistic microphysics schemes, such as, the Pardue Lin scheme (Chen and Sun 2002) and WSM6 (Hong and Lim 2006). While the warm-cloud Kessler scheme includes water vapor, cloud water, and rain, Pardue Lin and WSM6 recognize six classes of hydrometeors (water vapor, cloud water, rain, cloud ice, snow, and graupel), with certain differences between the last two schemes in ice-phase treatment. Some of the graupel-related terms in the WSM6 scheme follow the Pardue Lin scheme; still, these schemes differ in the ice phase, in which a single fall speed, which is weighted by the mixing ratios, is assigned to mixed-phase snow and graupel particles.

Due to the fact that the terrain slope, the length of the terrain slope, the terrain height and the location of the mountain relative to the coastline (Prtenjak et al. 2006; Crosman and Horel 2010) can affect SB development, the numerical experiments were performed with a modified topography. Here, this approach implies topography where the mountain heights of the Učka and Ćićarija Istrian Mountains (Fig. 1c) were reduced to 30% of their initial height (three tests per each case marked by MT; Table 1). This reduction in the mountain height and the percentage were chosen arbitrarily to obtain flatter terrain. This approach (see details in Appendix 1) allowed us to explain variations in the origin, timing and amount of convective activity on the evolution and dimensions of SBs.

The entire Adriatic Sea is a semi-enclosed sea with an average depth of 50 m in its northern portion. The area near the Istrian coast is even shallower, with a maximum depth of 30 m. The diurnal SST variations in shallow sea are relatively high (e.g., Sweeney et al. 2014), so the northern portion of the Adriatic exhibits great potential for investigating the effect of SST variations on the onset, development, characteristics and intensity of SBs and, consequently, convection. Therefore, the SST distribution has two representations in the model. A constant SST field from the ECMWF skin temperature analysis (Lin_MYJ in Table 1 for C1 case) was replaced by a varying SST field from hourly geostationary satellite data (Lin_MYJ_SST for C1 case). These much finer SST hourly data were obtained from the Meteosat Second Generation geostationary satellite and interpolated onto a 0.05° grid over the Adriatic, ensuring a gap-free SST data set (for more details see Prtenjak et al. 2015). The other parameters and model settings were unchanged.

2.4. Methods for Model Evaluation

We employed three approaches for this model evaluation since the use of the different validation approaches is useful (e.g., Mayor and Mesquita 2015) in giving an objective picture of the model performances. (1) Standard statistical parameters and (2) spectral representation (see Supplement 1) are verified by near-surface measurements. (3) The moment invariants in image analysis (e.g. Andrejczuk et al. 2003; Sović et al. 2013) were applied to the measured and modelled radar images (see Appendix 2) in order to objectively evaluate the spatio-temporal variations of the deep convection.

The following statistical measures were used in the standard statistical approach: bias (i.e., the mean deviation of the modelled data compared to that of the observed values; observations-model), the root mean square error (RMSE), the root mean square error after a constant bias has been removed (RMSD), the model standard deviation (St_dev_WRF) and the standard deviation from the measurements (St_dev_M). To evaluate the model performance, we used the same methodology as in Pielke (2002), Teixeira et al. (2014) and Prtenjak et al. (2015) when the evaluation of an acceptable mesoscale model skill could be achieved if the following comparison was satisfied: (1) St_dev_WRF $\sim$ St_dev_M, (2) RMSE $\lesssim$ St_dev_M, and (3) RMSD $\lesssim$ St_dev_M. Pairs from the observations and model were selected by using the nearest grid point of the model and considering the type of surface (i.e., land or sea) of the coastal stations.

The image moments analysis (IMA, Appendix 2) compare the maximum simulated radar reflectivity factor (dBZ) (only modelled radar reflectivity in Fig. 3) with observed radar images (from ARSO) particular model setup. The convective patterns are compared in time and space, thus avoiding problems in the direct pairing of in situ measurements with simulated values, e.g., the representativeness of the position measurements and the evaluation of the point

measurements with the average volume quantities in the model. Pattern-based methods (embracing spectral decomposition, principal component analysis, cluster analysis, etc.) have been widely applied as a validation tool (Beaver et al. 2010), and the IMA method has been used with radar (one variant examining the rainfall intensity in Andrejczuk et al. 2003) and satellite (Bellerby 2004) images. Our classification of radar echo patterns by the IMA method considers the shape and area of the radar reflectivity as well as the signal intensity in radar images. If the radar reflectivity from the model are closer to the observed sample then the

calculated parameter, the Euclidean distance (ED; Eq. 7) is smaller, which means smaller deviations between the model and observations.

3. Results and Discussion

3.1. Evaluation of the Model

3.1.1 In Situ Standard Statistical Approach

Figure 4 shows a diagnosis of the *spatial* comparison between the 10-m wind speed, 2-m rh and
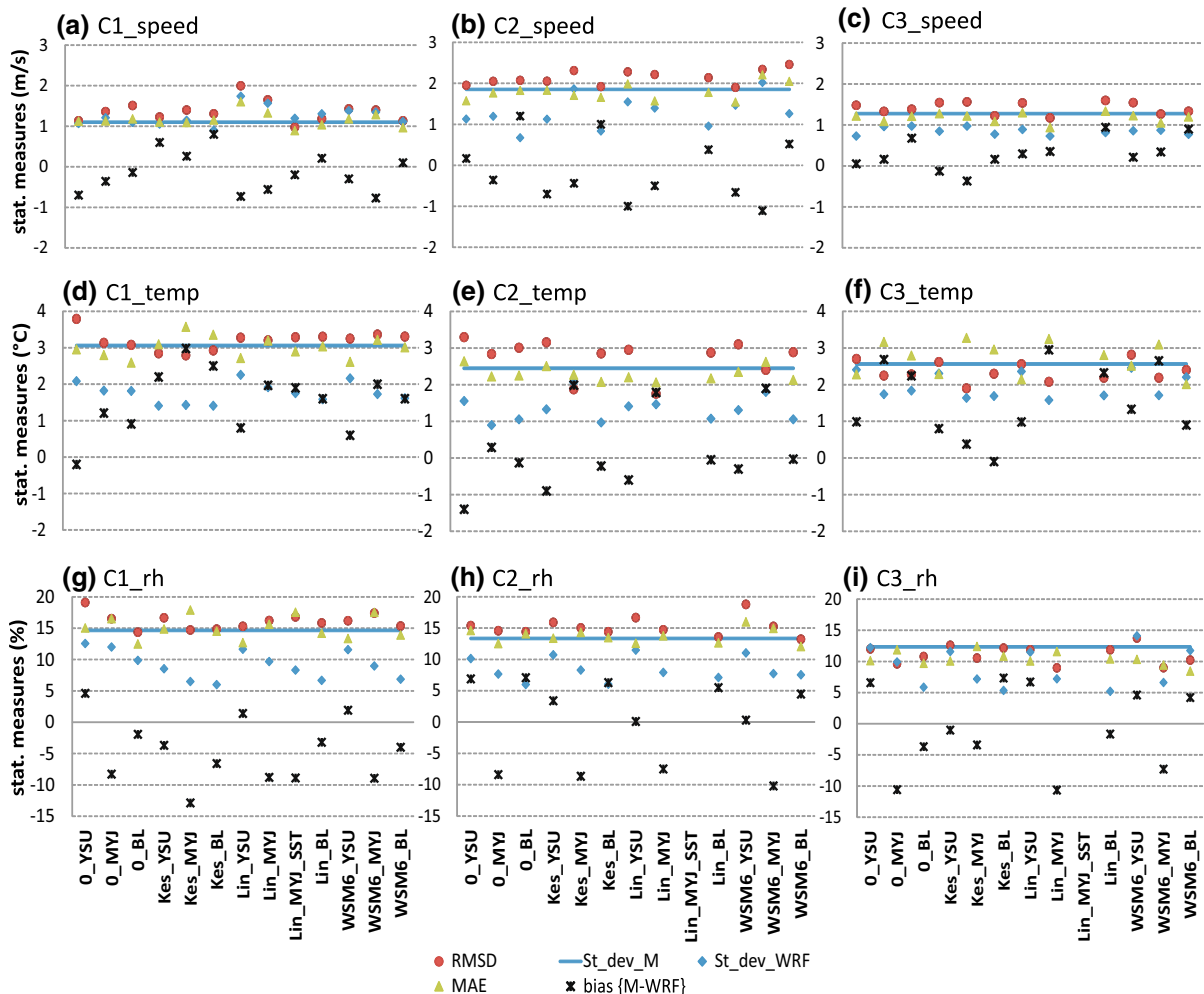

Figure 4

Statistical parameters [bias (observations-model, *black*), MAE (*green*), RMSD (*red*), standard deviations from both measurements and model, St_dev_WRF (*blue*) and St_dev_M (*blue line*), respectively; see text for details] for spatial model evaluation provided for 13 UTC (14 CET) using stations' data in Fig. 1. Statistics were calculated for all numerical experiments for all cases (*C1–C3*); **a–c** 10-m horizontal wind speed (m/s), **d–f** 2-m temperature (°C) and **g–i** 2-m relative humidity (rh [%])

temperature. Several statistical parameters (RMSD, MAE, St_dev_WRF, St_dev_M, and bias) for all the numerical tests (in Table 1) and all the selected cases for 13 UTC are shown. During the early afternoon, wind was adequately simulated in cases C1 and C3, with a somewhat inferior score for case C2 regardless of the model setup choice. The RMSDs were relatively low and approximately matched the St_dev_WRF and the standard deviations. The spatial distributions of the wind speeds indicated a reduction in biases with respect to the used ABL scheme. The best results were obtained by MYJ, followed by the BouLac scheme with a certain underestimation in the measured speeds. When using the YSU scheme, the afternoon wind speed was often overestimated. Generally, the MAEs for all the combinations were expectedly less than the RMSDs.

The schemes in the model setups also provided certain characteristic statistical properties in terms of the temperature. The biases were the largest for the MYJ scheme (regardless of the microphysics) and were predominantly positive (the model underestimated the temperature). The other two ABL schemes had lower biases, usually less than 1 °C (depending on the microphysics and cases), which occasionally changed the sign. The YSU scheme had the smallest positive or negative biases with certain microphysics options (implying the warmest ABL, Fig. 5).

According to the Cohen et al. (2015), the relatively low bias in the YSU scheme could be attributed to its ability to treat entrainment processes in a satisfactory manner within the ABL. The standard deviations in the model (St_dev_WRF) were uniformly less than the measured values although the matching was acceptable (Fig. 4). The RMSD values in cases C1 and C3 were comparable with the St_dev_WRF, except in the case C2, which generally agreed less with the temperature measurements.

The biases for rh were the lowest for the YSU scheme and the highest for the MYJ scheme regardless of the selected case. Positive bias dominated for the YSU scheme, while negative bias dominated for the MYJ scheme (i.e., the model overestimated the humidity). This result was accompanied by a decrease in the standard deviation values (St_dev_WRF) from YSU and MYJ to the BouLac schemes compared to the measured values (St_dev_M), which indicates the less successful performance of the model; the most in the case C1 and less in the other two selected ones. Smaller variability refers to the spatially homogeneous rh fields in the model. Generally, the RMSD was approximately equal to St_dev_M, except for the YSU scheme, which is distinguished by the greatest variations.

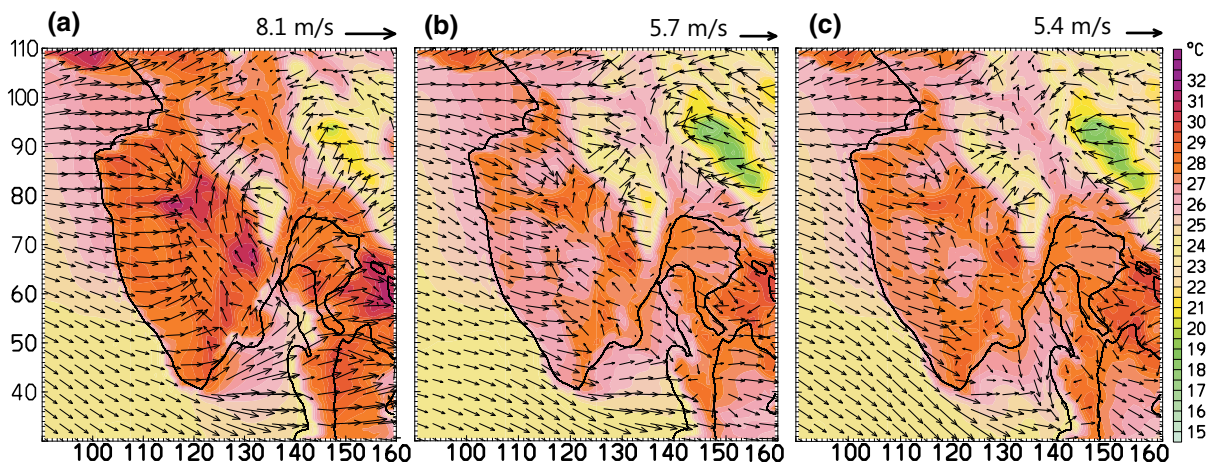Interestingly, the statistical parameters of the simulations without included microphysics had

Figure 5
Comparison of 10-m wind (m/s) and 2-m air temperature (°C) distributions over the target area for case C1 (9 July 2006) at 13 UTC (14 CET) without activated microphysics scheme: **a** 0_YSU test, **b** 0_MYJ test, **c** 0_BL test (see Table 1 for more details). The every third wind vector is depicted. The maximum reference vectors are different for each subfigure (*upper right corner*)

comparable values to the other numerical sensitivity tests (Fig. 4). This means that the deep convection which occurred in the area was rarely covered by measurements. Therefore, data from stations where SBs usually dominate, contributes to the final result of statistical parameters (see also Fig. 3). Furthermore, this approach revealed the behavior of each ABL scheme itself; from a warm and dry ABL in the nonlocal YSU scheme to a cold and moist ABL in the local MYJ scheme (Fig. 5), with the local BouLac scheme between these two extremes. This statement is consistent with the conclusions of Weisman et al. (2008) and Milovac et al. (2016), who noted that the YSU scheme creates a warmer, less humid and much deeper ABL that rapidly grows and aggressively removes a layer of inversion compared to the MYJ scheme. When using the YSU scheme, the faster drying of the lower ABL (compared to local schemes) indicates higher mixing properties (Milovac et al. 2016). The MYJ scheme usually produces the most humid and, consequently, the least convective ABL and an excessively thick inversion layer, which influences the dew point temperature and lowers the lifting condensation level. This result indicates higher potential for cloud development. However, according to Milovac et al. (2016), nonlocal schemes produce excessively fast ABL evolution, during which the ABL height from nonlocal schemes fits worse than that from local schemes.

Although the statistical parameters of the near-surface variables did not display significantly unrealistic results, the lowest temperature was reached in the simulations that used the Kessler scheme (not shown). The Kessler scheme often underestimated the wind (see biases in Fig. 4), and the best result was obtained for the case C3, which had the weakest and the most local convection. Generally, the more complex microphysics schemes (Pardue Lin and WSM6) had better scores for particular ABL scheme. However, all microphysics schemes were mostly inferior when combined with the YSU scheme in the model setup.

We calculated a simple index (s) as average values from three selected cases to evaluate scattering of some statistical parameters (Table 2): $s = \frac{M-m}{m} \times 100\%$. The maximum ($M$) and minimum ($m$) values of the errors (MAE and RMSD) were used for a given

Table 2

Scattering of the results in different combination of microphysics and ABL schemes was estimated as average of cases according to the formula: scattering $(\%) = \frac{M-m}{m} \times 100\%$ *taking into account maximum (M) and minimum (m) value for particular scheme for data in Fig. 4 at 13 UTC for wind speed (V, m/s), temperature (T, °C) and relative humidity (rh, %)*

	Scattering of microphysics scheme (%) for fixed ABL scheme			Scattering of ABL scheme (%) for fixed microphysics		
	YSU	MYJ	BouLac	Kessler	Lin	WSM6
MAE_speed	32	20	25	21	37	26
RMSD_speed	27	31	23	11	41	31
MAE_T	11	24	8	37	31	20
RMSD_T	16	15	21	27	25	33
MAE_rh	14	13	12	14	20	36
RMSD_rh	16	18	15	18	16	29

set of ABL and microphysics schemes (in Fig. 4). According to the relative scattering (s), the near-surface modelled results depended more on the temperature and rh in terms of the selected ABL scheme compared to the microphysics. The simulation of the 10-m wind speed was equally influenced by both options (ABL and microphysics); however, choosing the ABL scheme played a major role in simulating wind speeds for the Pardue Lin option. Although the temperature from the MYJ scheme was the most sensitive to the selected microphysics, the results had minimal dependence on the selected microphysics if the BouLac scheme was used.

When the Kessler scheme was applied, the scattering of the results, s, in terms of the rh and wind speed, was less than 20% regardless of the ABL scheme. The relatively poor results from the Kessler scheme were very consistent, which is evident from its small s. Due to the fact that the dynamics of the model provided a completely different results compared to the measured values, it can be concluded that a certain "systemic" error existed.

The evaluation of the model *in time* is shown in Fig. 6, which represents the bias, MAE, RMSD and standard deviation between each experiment (in Table 1) and measurement for the Pula station in case C2. Despite the relatively weak observed wind speeds (when the models reproduced the flow less correctly), the wind speed at Pula station was
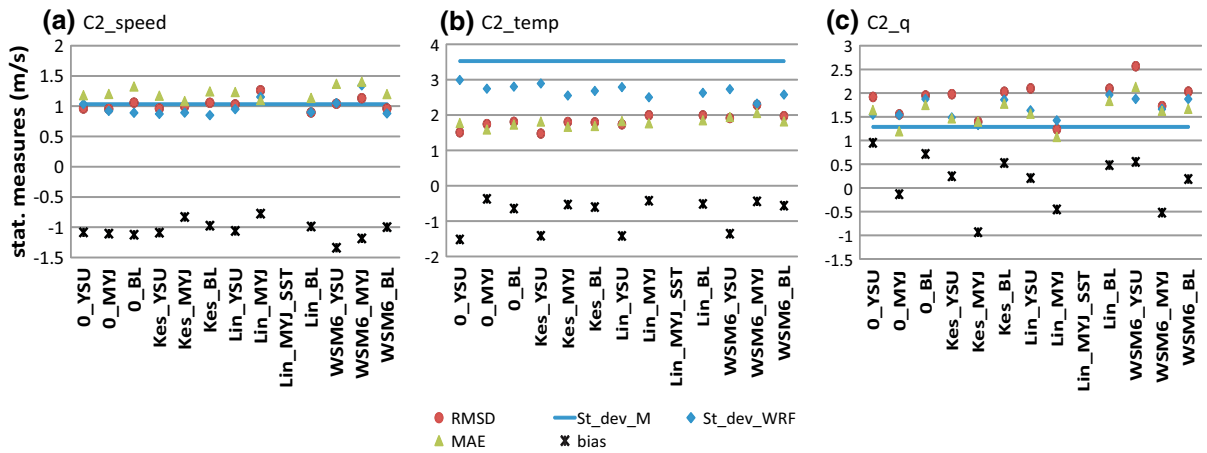
Figure 6
Statistical parameters [bias (*black*), MAE (*green*), RMSD (*red*), standard deviations from both measurements and model, St_dev_WRF (*blue*) and St_dev_M (*blue line*)] for model evaluation in time at Pula-airport station (Pula-A in Fig. 1). Shown for entire C2 case (8 August 2006) and for all numerical experiments (in Table 1); **a** 10-m wind speed; **b** 2-m temperature, **c** 2-m mixing ratio

simulated quite well regardless of the model setup (with comparable standard deviations and RMSDs between the model runs and measurements). The biases only showed small variations among different model options, with the smallest one for the Lin_MYJ setup. Although the temperature was also adequately reproduced (visible through the comparison of statistical errors), the YSU scheme proved to be a poor choice here. The mixing ratio [*q* (g/kg)],

which was calculated by rounding the METAR values, indicated less matching in the time series between the model runs and measurements. According to the largest biases (i.e., negative values, indicating the most humid lowermost atmosphere), the comparisons among the standard deviations and statistical errors according to Pielke (2002), were the best when the MYJ scheme was used (in particular, Lin_MYJ).
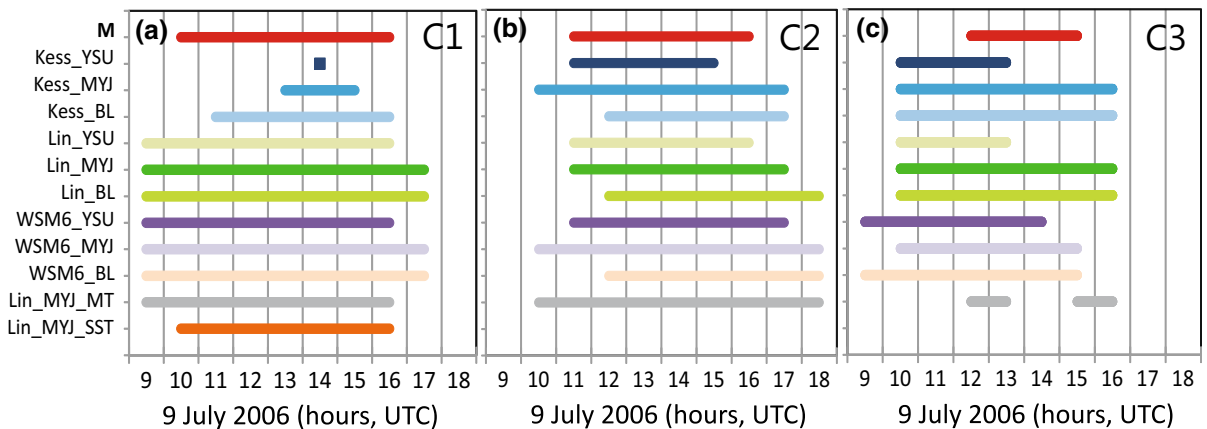

Figure 7
The onset, decay and duration of convective activity over the area of interest in all three selected cases (9 July 2006, *C1*; 8 August 2006, *C2*; 8 June 2003, *C3*) for all runs which are using microphysics option (see Table 1). The abbreviation *M* stands for measurement and other abbreviation are described in Table 1 according to the different model setup
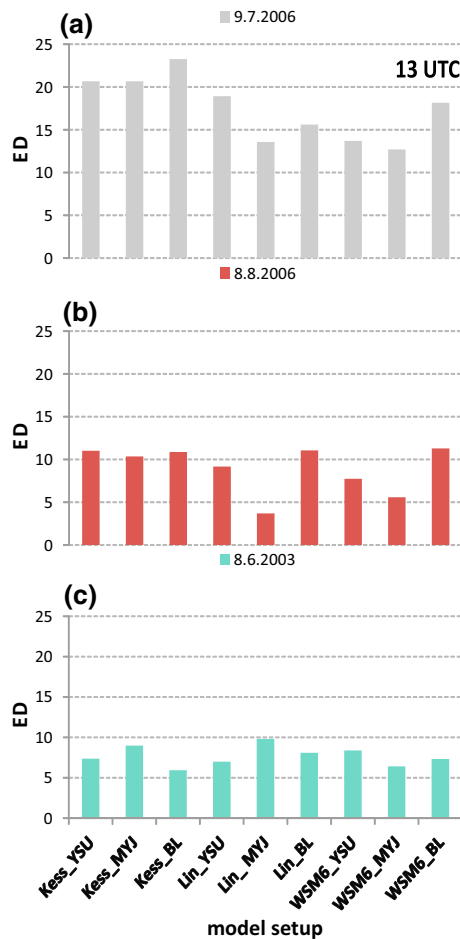
Figure 8

The image moments analysis method applied on all three selected cases (9 July 2006, *gray*; 8 August 2006, *red*; 8 June 2003, *green*) at 13 UTC (14 CET) for runs which are using different microphysics options (see Table 1). The model is more successful when the Euclidean distance (ED, Eq. 7) is smaller, which means that the model is closer to reality

3.1.2 Moment Invariants Approach

Figure 3 represents the simulated composite reflectivity accompanied by the 10-m wind in the smallest model domain, which shows the interaction of SBs and thunderstorm cells for case C1. Every subplot displays one particular model setup at 13 UTC (14 CET) over Istria. According to the radar images, the lifespan of the observed storms ranged from 10 to16 UTC in C1 (Fig. 7a). Figure 7 also displays the onset and decay (i.e., duration) of the convective activity in nine model setups for each case. In cases C2 and C3 (Fig. 7b, c), the duration of

the thunderstorms ranged from 11 to 16 UTC and from 12 to 15 UTC, respectively.

At first glance, the Kessler scheme obviously provided very poor results, significantly underestimating the observed deep convection in space (Figs. 2, 3). The variations between complex microphysics schemes (Pardue Lin and WSM6) were relatively small, with somewhat stronger convection in the WSM6 scheme, showing that the position and intensity of convection largely depended on the chosen ABL scheme. This result describes the important role of the surface-atmosphere interactions, which control the transfer of momentum, heat and moisture as the main source of water vapor in the atmosphere (e.g., Janjić 1994; Teixeira et al. 2014; Kleczek et al. 2014). Therefore, the YSU scheme in case C1 failed to reconstruct the deep convection over the mountainous part of Istria at 13 UTC, and BouLac failed to simulate convective cells along the convergent zone in the central portion of the peninsula. The MYJ scheme had the best performance in this case, despite the similar duration of convective activity in terms of the other model setups (Fig. 7a).

An application of IMA method is shown in Figs. 8 and 9 (and Fig. S1.3 in Supplement 1) and displays the success of all the schemes in a quantitative manner. During a well-developed deep convection at 13 UTC (Fig. 8), the EDs were (generally) larger for the Kessler option and smaller for the more complex schemes regardless of the ABL scheme, which is particularly obvious for case C1 (Fig. 8a). Among the different combinations, the Lin_MYJ case showed very good agreement between the modelled and measured deep convection coverage, producing relatively small ED in accordance with Fig. 3.

In Fig. 9 (and Fig. S1.3), the Lin_MYJ combination revealed that smaller ED values mostly occurred in the beginning and ending convective hours, while the increasing number of convective cells in the domain (up to 14 UTC) also caused the ED to increase. However, small ED values (i.e., high realism) can form from a variety of reasons. At the beginning of the examined period, only modeled and no observed small convective cells were present in most of the model setups (Fig. 7), which means that the model created earlier initial convection. According to the observed lifespan of convection, which
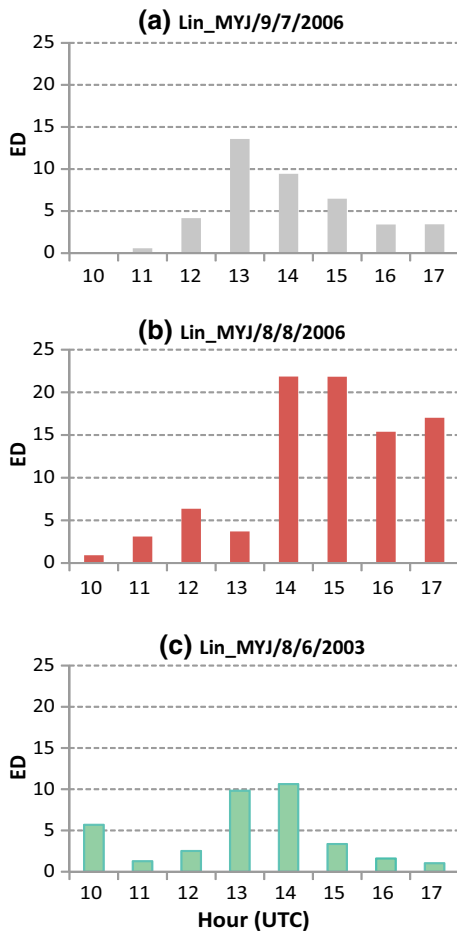
Figure 9

The image moments analysis method applied on all three selected cases (9 July 2006, *gray*; 8 August 2006, *red*; 8 June 2003, *green*) from 10 to 17 UTC for numerical runs which are using Lin_MYJ options (see Table 1). The model is more successful when the Euclidean distance (ED, Eq. 7) is smaller, which means that the model is closer to reality

ended after 16 UTC, the model also showed prolonged non-existent Cb cells. Both cases corresponded to false alarms. However, these terms should be taken with a certain caution. The resulting EDs can only be compared to those that are obtained for inputs with similar signal content if the signal in the input image is small (unfavorable signal-to-noise). Some calculations showed that the threshold was approximately 10% of the signal that was contained in the input image (Demoli et al. 2013).

Additionally, the results of "mixed physics" revealed several features in the early afternoon hours during intense convection (see Fig. 8, S1.3). First, the

Kessler scheme was not entirely appropriate because this scheme produced relatively large ED values by underestimating the observed convection (in coverage, intensity and duration; see also Fig. 7). However, this disagreement was lower in cases C2 and C3 (Fig. 8). Second, more complex microphysics schemes indicated better matching in general. Still, complex schemes exhibited certain underestimation of the mature convection when using the nonlocal YSU scheme. The YSU scheme also provided short-term convection (Fig. S1.3), with a lack of stratiform cloudiness during the final stage (not shown). In the late afternoon hours, opposite could be observed for the local ABL schemes which showed overestimated convection for all the parameters, particularly for cases C1 and C2 (Fig. 8, S1.3). The observed overestimation was more pronounced in the MYJ than in BouLac schemes using the WSM6 rather than Pardue Lin schemes. However, unrecognized convection in the model is a greater error than the overestimated intensity of observed convection, which implies that the Pardue Lin scheme, showed acceptable characteristics as the microphysics scheme.

3.1.3 Model Setup and SB Characteristics

Miao et al. (2009) showed that the effect of ABL schemes on the simulations of SB onset, evolution and speeds (which are controlled by the sensible heat flux, HF) and the intensity of vertical SB circulation (which is mostly controlled by stability) could be significant. Therefore, the local SB characteristics for the three ABL options are shown for the Lin microphysics scheme for case C1 (Table 3). In all three ABL variants (Lin_YSU_C1, Lin_BouLac_C1, and Lin_MYJ_C1), the SB had a typical spatial structure of a gravity current (not shown). By midday, the temperature over the peninsula has increased by 3–4 °C compared to the SST, depending on the ABL scheme (as in Fig. 5). The differences among the ABL schemes were noticeable in the heights of both the SB body and SBF, indicating the largest values for the YSU scheme, and typically lower in the other two ABL schemes (Table 3). The height differences were associated with differences in the maximum SB speed. The SB speeds in the YSU scheme exceeded 7 m/s, while the maximum SB speeds in the other

Table 3

Sea breeze (SB) characteristics observed along the vertical cross-section B1B2 (Fig. 1) averaged in time (between 09 and 13 UTC) for chosen simulations over the Istrian peninsula

	Parameters in vertical cross-section (averaged for 10–13 UTC period)			
	SB inland penetration (km)	SB body height (m)	SBF height (m)	SBF updraft (cm/s)
CASE				
Lin_YSU _C1	18	800	2300	150
Lin_BouLac__C1	14	500	1900	113
Lin_MYJ_C1	15	600	2075	140
Lin_MYJ_MT_C1	9	440	1760	64
Lin_MYJ_C2	20	350	1460	138
Lin_MYJ_MT_C2	16	330	1440	111
Lin_MYJ_C3	27.2	400	1460	93
Lin_MYJ_MT_C3	27	400	1380	115

The inland penetration of the SB and the height of the SB front (SBF) are determined by the position of the SBF updraft

two schemes were approximately 5 m/s. These results also match the greater (YSU)/smaller (MYJ, BouLac) HF, greater buoyancy in the ABL, higher mixing and higher (YSU)/lower (MYJ, BouLac) ABL heights, which are largely consistent with the results from many previous ABL studies (e.g., Cohen et al. 2015; Milovac et al. 2016). Consequently, the SB's inland penetrations (especially those from the western coast) were different: earlier, faster and farther penetration was present using the YSU scheme and later, slower and shorter with the other two ABL schemes (Table 3). Cohen et al. (2015) argued that these local schemes can have a substantial disadvantage regarding their depiction of the PBL because the tops of the simulated daytime ABL entrainment processes are less accurately represented. However, the local ABL schemes in this study were more correct on average, in contrast to Cohen et al. (2015) and also to Challa et al. (2009), who stated that the YSU scheme shows improvement over the MYJ scheme when simulating SBs.

The dimensions and speeds of SBs vary considerably for different microphysics scheme. For the Kessler scheme, SBs were not identifiable (see Fig. 3) because of large bias in the cloud cover (not shown). The relative simplicity of the parameterization of the convection was obviously not

acceptable for this resolution and this complex terrain. For more complex microphysics, afternoon convection had a destructive effect on the appearance and evolution of SBs, indicating a negative feedback relationship. While the SB from the western peninsula's coast and large convergence zone only "survived" in the Lin_YSU test after convective activity, deep convection destroyed the afternoon SB in the Lin and WSM6 schemes. Clouds, cold and strong low-level downdrafts (which diverged under the clouds), and precipitation decreased solar irradiance and the afternoon temperature gradients between the land and sea (Poljak et al. 2014), which caused the SB to vanish and large-scale wind to dominate.

SB–Cb interactions are sensitive to the used schemes and parameterizations in numerical simulations. The overall evaluation suggested no simple selection; however, the Lin_MYJ model setup had certain advantages over the others. Therefore, this setup is used in the following numerical experiments.

3.2. Simulations with Modified Topography and Different SST Fields

3.2.1 Modified Topography

Topographically driven deep convection and consequent precipitation greatly depend on the wind speed and direction, therefore the changes in the wind field that are forced by the topography could be observed up to the lowermost 4 km (e.g., Teixeira et al. 2014). Because of abrupt changes in the surface-energy balance (e.g., Barthlott and Kirshbaum 2013), interactions between mountain and coastal circulations can affect the initiation and development of convection. This phenomenon is particularly expressed if the SB and slope/valley winds fall roughly into phase, during which these two circulations will combine to strengthen their inland propagation. However, high mountains can diminish the penetration of maritime air by SBs due to mechanically blocking (e.g., Prtenjak et al. 2008). Therefore, the influence of the large mountains of the peninsula on SB–Cb interplay was tested here by performing sensitivity tests with modified topography (see Table 1).
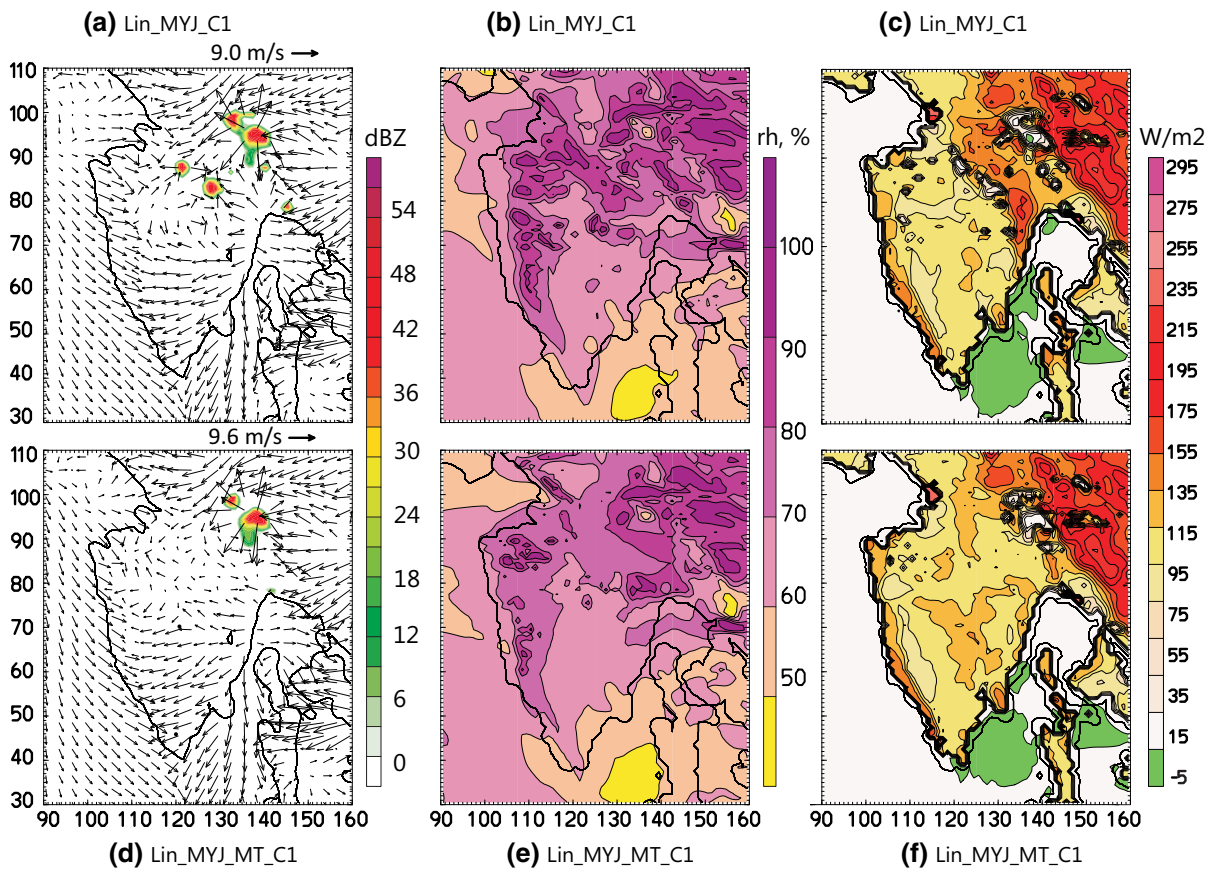
Figure 10

The modelled results on 9 July 2006 (*C1* case) at 09 UTC in the tests with **a**–**c** original and **d**–**f** modified (MT) topography; **a**, **d** the modelled 10-m wind agl (in m/s) and the maximum simulated equivalent radar reflectivity factor (dBZ); **b**, **e** averaged relative humidity (rh, %) between 850 and 500 hPa; **c**, **f** surface heat flux (W/m²). In **a**, **d** every third wind vector is presented and maximum reference vectors are different for each subfigure (*upper right corner*)

Figure 10 (09 UTC) and 11 (13 UTC) showed the modeled 10-m wind and the maximum simulated equivalent radar reflectivity factor (dBZ) of numerical tests with original and changed topography for C1 and C2 cases. In Fig. 10 average rh between 850 and 500 hPa levels and surface HF distributions, as fundamental driver of the SB (Crosman and Horel 2010) are displayed.

The first Cb cells in the Case C1 developed because of larger-scale air lifting along the northern (windward) slopes of Istria's mountains ($x \sim 130$–140 and $y \sim 80$–100 in Fig. 10a). The Cb cells propagated towards the downslope side (i.e., to the southwest), providing the rapid development of new convective activity over the central part of

peninsula. One hour later (not shown) on the leeward side of the mountain, these Cb cells produced several spots with a total precipitation of 15 mm. However, the corresponding MT case ($x \sim 130$–140 and $y \sim 80$–100 in Fig. 10d) showed weaker storm development, indicating a smaller number of convective cells and differences in their size. In time, these Cb cells developed later and provided less precipitation (e.g., ~ 11 mm at 10 UTC) for the MT case.

These differences in the initial convective activity occurred because of the changes in (1) the lowermost wind regime and humidity advection and (2) the mid-tropospheric humidity (850–500 hPa; Fig. 10b, e). When the terrain was higher (steeper slopes enhance

terrain forcing and cause stronger air lifting), the mid-troposphere was more humid ($x \sim 130$–140 and $y \sim 80$–100 in Fig. 10b, e), which agrees with the results of Barthlott and Kirshbaum (2013) and Teixeira et al. (2014). Reducing the height of the mountains (in the MT case) on the upwind side ($x \sim 140$ and $y \sim 90$ in Fig. 10c, f) values of HF were lower (~ 50 W/m^2). This caused that the western SB flow initiated 1 h later with lower penetration ($x \sim 110$ and $y \sim 50$–90 in Fig. 10a, d), somewhat lower speeds and lower heights of the SB body and SBF (Table 3). The same was observed for the morning eastern onshore flow from Rijeka Bay ($x \sim 140$ and $y \sim 70$–90 in Fig. 10a, d) where weak eastern SBs formed (instead eastern slope-SB winds in Lin_MYJ_C1 case). It contributed to limited moisture advection over coastal area in the wider Rijeka area (where the Učka height was reduced; $x \sim 140$ and $y \sim 80$). The SB was weak because of the unfavorable NE large-scale wind direction and the concave shape of the coast, which caused the flow to diverge.

Although, the low-level q within the SB body had higher values in the LIN_MYJ_MT_C1 case, (not shown), the humidity advection was more pronounced in LIN_MYJ_C1 case. Mountains have contributed to the air lifting along the slopes, which transferred even more moisture to the mid-level troposphere and retained the stationary inflow of moisture in the higher layers. The moisture was also better transferred to the mid-level troposphere because of the larger and stronger updrafts (Table 3) at the SBF in the LIN_MYJ_C1 case.

An analysis of the convective indices at 09 UTC affirmed that the highest values of CAPE [1804 J/kg (Lin_MYJ_C1) vs. 1923 J/kg (Lin_MYJ_MT_C1)] over the peninsula were found in the region of the convergence zone and were connected to the lower near-surface moisture (q values), as suggested by Barthlott and Kirshbaum (2013). The largest values of CIN [76 J/kg (Lin_MYJ_C1) vs. 63 J/kg (Lin_MYJ_MT_C1)] were found in the mountainous (modified) region, which coincides with the region of the initiated deep convection (not shown). Decreasing the terrain height increased the CAPE and decreased the CIN in the domain compared to Lin_MYJ_C1. The variability occurred mostly because of enhanced moisture in the lowermost air

and reduced air mixing. Additionally, the higher lifting convergence level and the level of free convection compared to the Lin_MYJ_MT_C1 case revealed that a strong trigger contributed to the occurrence of deep convection along the convergence zone.

In time, the convective cells in both cases produced strong downdraft outflows (still somewhat weaker in the Lin_MYJ_MT_C1 case with a delay), which formed secondary cells along the main convergence zone after collision with the SBF ($x \sim 120$ and $y \sim 50$–75 in Fig. 11a, b). The higher terrain produced stronger convective afternoon storms with stronger rainfall, while the Cb cell's growth in the flatter terrain was still weaker and delayed (in agreement with all the mentioned values). This result coincides with the result of Wang et al. (2013). After 14 UTC, the convective activity of both runs began to decay.

Similarly to C1 case, thunderstorm was weaker and delayed in C2 case with modified topography. The analysis of the case C2, indicated that the two significant convective activities were developed at two different regions ($(x, y) \sim$ (130, 60) and (150, 100) in Fig. 11c). Both of them were simulated at the same time in unmodified and modified cases (Fig. 11c, d) but with the different intensity and somewhat different location. The differences appeared at the NE of Istria in both cases, due to the surface convergence and less organized onshore flow in Lin_MYJ C2 case ($(x, y) \sim$ (150, 100); Fig. 11d). Due to stronger blocking effect of the northern mountains and higher mid-tropospheric humidity in the Lin_MYJ_C2 case over the elevated Učka and center of peninsula ($(x, y) \sim$ (130, 60); Fig. 11c), convection was characterized with the higher number of convective cells, stronger updrafts and higher total precipitation than in the Lin_MYJ_MT_C2 case. One of the reasons is the stronger near-surface convergence in unmodified terrain (Lin_MYJ_C2). Delayed convective cells over the main convergence zone in Lin_MYJ_MT_C2 produced weaker updrafts (Table 3) and consequently weaker convection compared to the case Lin_MYJ_C2 (Fig. 11c, d). This is pointing out much more favorable pre-convective conditions in the Lin_MYJ_C2 case which had an influence on the
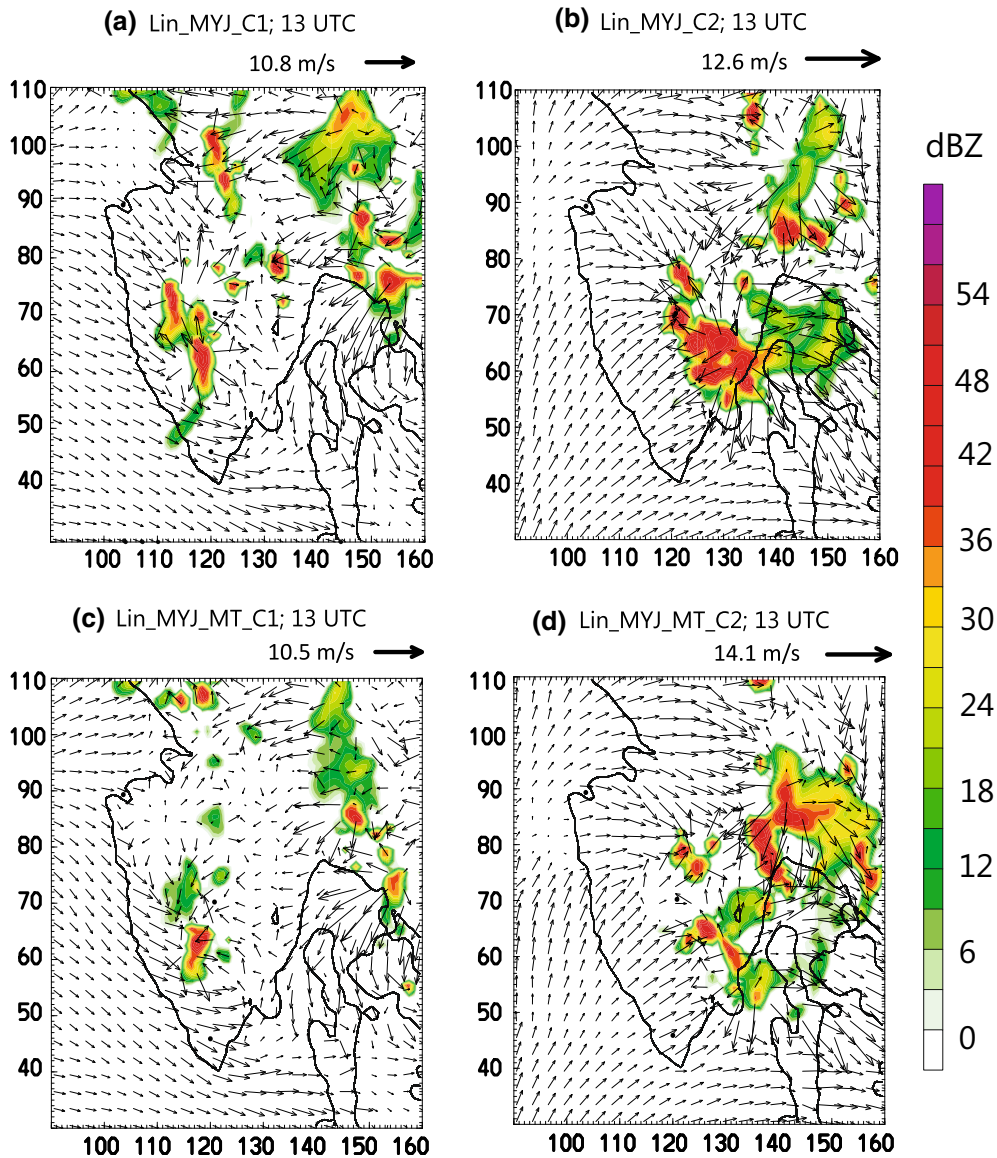
Figure 11
The modelled results on 9 July 2006 (*C1* case) and 8 August 2006 (*C2* case) at 13 UTC in the tests with **a**, **c** original and **b**, **d** modified topography; the 10-m wind agl (in m/s), and the maximum simulated equivalent radar reflectivity factor (dBZ) with *legend on the right*. Every third wind vector is presented and maximum reference vectors are different for each subfigure (*upper right corner*)

stronger and earlier development of the following convection along the convergence zone. The differences between the onshore SBs characteristics from the both cases are rather visible after 11 UTC. Due to the lower HF in the whole peninsula (by ∼ 45 W/m², as in Fig. 10b, e for case C1), the western SB in the Lin_MYJ_MT_C2 case had smaller inland intrusion (∼ up to 14 km), while dimensions of SB and SBF

front were quite similar in both tests (Lin_MYJ_C1 and Lin_MYJ_SST_C1). The convergence zone was again accompanied by the highest values of CAPE, whereas both the CAPE and CIN showed the same relationship as in C1 (the higher the topography, the lower the values of CAPE and CIN).

Due to the fact that the case C3 was already presented as the relatively short and weak

thunderstorm case, the influence of the modified topography was rather weak. However, some of the similarities with the other two above mentioned cases were noticeable: (1) the delayed and less intensified convective activity over peninsula, (2) the smaller amounts of the precipitation in the Lin_MYJ_MT_C3 case and (3) the same relationship between the values of the CAPE and CIN. The averaged rh in the mid troposphere is relatively low in both of the cases (<40%), indicating somewhat higher values in the Lin_MYJ_C3 due to the higher topography. Contrary, the high low-level humidity in Lin_MYJ_C3 case caused by the advection of the humid air from the sea (supported by the southerly ambient onshore winds and SB mechanism) was even higher in the Lin_MYJ_MT_C3 case. Still, differences between SB and SBF characteristics for both modified and unmodified terrain were less detectable compared to the C1 and C2 cases (Table 3).

Based on these three cases, analysis showed that lowering the height of the mountains affected the local flow by creating an eastern SB (nearby Rijeka Bay) and intensifying the SB in the Gulf of Trieste. The SBs contributed to the marine air advection over land, creating a more humid ABL over the peninsula. Although the intensity of this modification depended on the large-scale wind direction, the overall effect was relatively minor and mostly local in the entire wind field. The mountains blocked the deeper penetration of marine air over the peninsula but also generated jointed anabatic-SB wind, which increased the mid-tropospheric humidity and thus accelerated and intensified the convection in the area. This effect was even more pronounced for large-scale flow from northern directions. Furthermore, the effect of the Cb formation caused by forced convection on the mountain slopes surpasses the effect of moisture advection by SB, accelerating and intensifying convection.

3.2.2 SST Variations

Analyzing SST influence, two tests were made. A static spatial SST field in Lin_MYJ_C1 case was completely based on ECMWF input and therefore, burdened with the error from this coarse model. The SST distribution in Lin_MYJ_SST_C1 was much more realistic based on satellite data.

The spatial statistics (when considering the low-level wind fields (Fig. 4) at 13 UTC of both tests: Lin_MYJ_C1 and Lin_MYJ_SST_C1), revealed that more precise SST data somewhat improved overall model performance. The statistical parameters did not change for the temperature and only slightly weakened in the humidity reconstruction. This result is somewhat expected because modifying the SST along the coast was sporadic and did not significantly affect the spatial statistics further over land. However, the results from the Lin_MYJ_SST_C1 run at several coastal stations always better matched the values from the observations (not shown). Still, errors caused by different model setup surpass the model errors due to less correct SST field defined in the model.

Both sensitivity tests were compared with observed data for C1 case. The Lin_MYJ_C1 case revealed somewhat earlier (Fig. 7) and spatially less accurate convective activity than the Lin_MYJ_SST_C1 case (Fig. 12a–c). Thunderstorm cells began to develop within the main convergence zone in Lin_MYJ_C1 (but not in the radar images), with the simultaneous development of mountain convective cells in the NE portion of the peninsula in both simulations ($(x, y) \sim (14°E, 45.5°N)$ in Fig. 12a–c). In time, the convective activity was better reproduced in the Lin_MYJ_SST_C1 case, although still with some deviation. In both runs, the generated storm cells decayed during the afternoon (Fig. 7), mainly in accordance with the observations. The total amount of precipitation in the Lin_MYJ_SST_C1 case and its spatial arrangement also indicated better spatial compliance with the measurements than those in the Lin_MYJ_C1 case (not shown).

Being larger in Lin_MYJ_C1 case than in Lin_MYJ_SST_C1 run, HF (Fig. 12d, f) and SST (Fig. 12g, i) near the western Istrian coast ($x \sim 13.5°E$, $y \sim 45°N$–$45.5°N$) differs up to 15 W/m^2 and up to 2.5 °C (up to 11 UTC and later), respectively. The HF, which established the land–sea temperature difference, can markedly affect the modification of the ABL properties (Miglietta et al. 2011), the onset, development and intensity of SBs, and the low-level convergence that generated the convection (Crook 2001). Prtenjak et al. (2015)
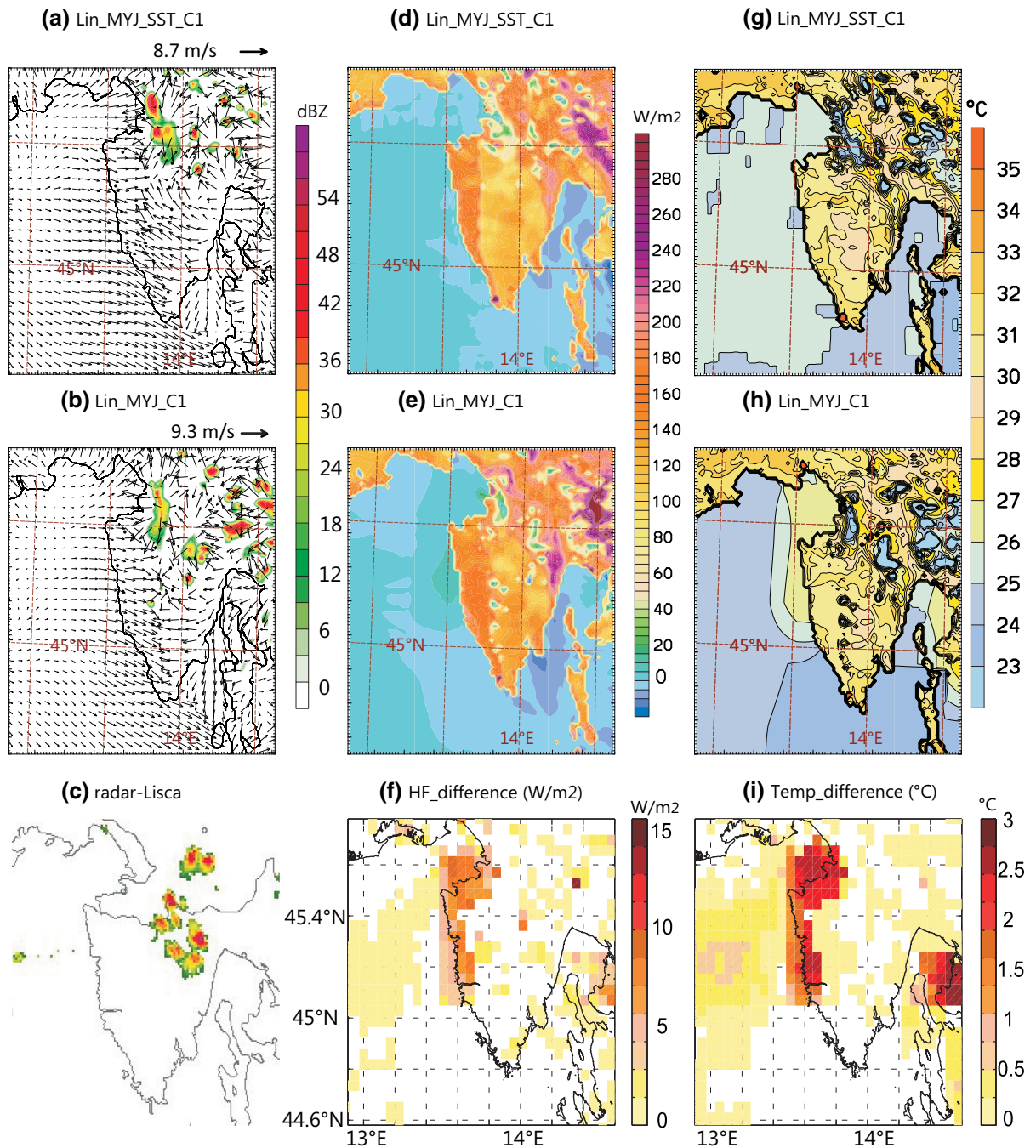
Figure 12
The modelled results on 9 July 2006 (*C1* case) at 11 UTC in the tests with **a**, **d**, **g** satellite SST and **b**, **e**, **h** ECMWF_SST constant data; **a**, **b** the modelled 10-m wind agl (in m/s) and the maximum simulated equivalent radar reflectivity factor (dBZ), **c** radar data (source: ARSO-http://www.meteo.si), **d**–**f** modelled surface heat flux distributions (W/m²) in both SST runs and their difference (Lin_MYJ-Lin_MYJ_SST) and **g**–**i** modelled skin temperature fields (°C) in both SST runs and their difference (Lin_MYJ-Lin_MYJ_SST)
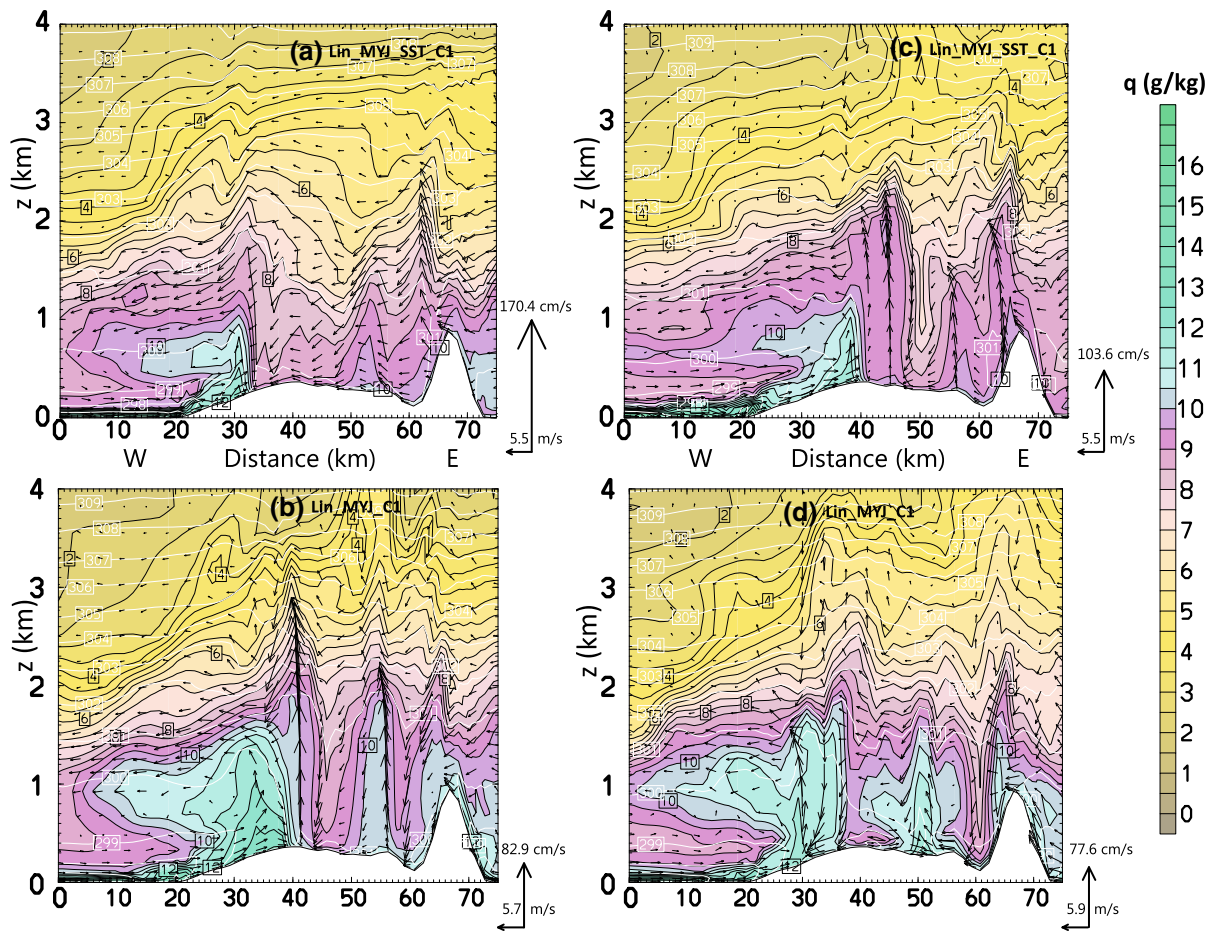
Figure 13
Vertical cross-sections along the BB1 line in Fig. 1 on 9 July 2006 (*C1* case) at **a**, **b** 11 UTC and **c**, **d** 13 UTC with variable SST fields in **a**, **c** Lin_MYJ_SST_C1 case and **b**, **d** constant SST in Lin_MYJ_C1 case. Potential temperature (°C, *white lines*), the mixing ratio (g/kg, *filled colored areas*) and the tangential components of wind vectors (m/s) which are represented by *black arrows* with maxima vectors *on the right*

examined the influence of a constant, coarsely resolved SST field on the refractive conditions in this area and analyzed potential errors (i.e., artificial warming of the sea near the NW Istrian coast). These authors found that summer SST variations of a few degrees affected the structure of the marine ABL to 700 m. The positive SST and HF differences (Fig. 12f, i) between the Lin_MYJ_C1 and Lin_-MYJ_SST_C1 runs contributed to the stronger development of SBs (in Lin_MYJ_C1) during the morning hours (Fig. 13a, b). Convection formed earlier and developed faster because of the faster developed SB during the earlier stage (which contributed to the transport of higher humidity in the boundary layer, Fig. 13b) and larger generated heat

fluxes in the Lin_MYJ_C1 run. After 11 UTC, the already strongly developed convection along the convergence zone induced a negative feedback on the further development of the SB in this run. In contrast, the penetration of the SB flow and other characteristics of the SB were more emphasized in the Lin_MYJ_SST_C1 run during this period: the heights of the SB body and SBF were generally higher (compared to the Lin_MYJ_C1 run), which clearly showed that slower and somewhat weaker convection contributed to the improved development of the SB (Fig. 13c, d). The convergence across the SBF in the Lin_MYJ_SST_C1 run after 11 UTC increased ($\sim -1.8 \times 10^{-3} \text{ s}^{-1}$) compared to the Lin_MYJ_C1 run ($\sim -1.6 \times 10^{-3} \text{ s}^{-1}$), so the

vertical speeds within the updrafts were higher, which induced somewhat stronger deep convection in this case. High values of CAPE could be recognized within the convergence zone in both runs, with higher values in Lin_MYJ_SST_C1, because of the moistening of the low-level air layer during the SB's inland penetration and the appearance of heat and moisture surface fluxes.

The quantity and distribution of humidity in the boundary layer of the convergence zone and in the middle layers of the troposphere can greatly affect the onset, intensity and development of storms (Crook 1996), so the mixing ratio in the boundary layer and mid-tropospheric rh are also shown in Fig. 13. The moistening of the low-level marine ABL increased the humidity in the SB body because of the higher SST that was produced in the sensitivity test with constant SST. This phenomenon is the most likely reason why the convection in the Lin_MYJ_C1 run was more intense and more developed before noon and also coincided with the results of Miglietta et al. (2011). These authors stressed the positive feedback relationship between the SST and convection, in which warmer SST and stronger sea-surface fluxes accelerate and enhance the development of convection. However, this relationship is only one effect in the non-linear interactions between SBs and Cbs.

Observations of the mid-tropospheric humidity also revealed somewhat higher values for the Lin_MYJ_C1 run until 10 UTC (not shown). However, the values of each variable abruptly increased for the Lin_MYJ_SST_C1 run after 11 UTC (Fig. 13), which shows that the more strongly developed SB and horizontal advection of the humid marine air at this point ($\sim 1.6 \times 10^{-3}$ g/kg more than in Lin_MYJ_C1) could have contributed to the higher humidity in the mid-tropospheric layers. On the other hand, the higher convergence and more strongly developed updrafts in the Lin_MYJ_SST_C1 run along the SB front transferred humid air into the higher layers of the troposphere, which indicates stronger vertical penetration and the "feeding" of the Cb cells with moisture. This phenomenon could also be one of the main causes of the somewhat stronger convection and higher amounts of precipitation in this case.

4. Summary and Concluding Remarks

In this study, we examined the sensitivity of the interactions of SB and Cb on the mixture physics, topography height and SST field variations. Three weather patterns that are relatively frequent during the warm season and are associated with air-traffic problems (9 July 2006; C1, 8 August 2006; C2 and 8 June 2003; C3) were simulated by the WRF model and evaluated by available data and different validation methods. Numerical experiments were performed from a total of 43 simulations with (1) mixed physics, which involved 13 combinations of microphysics (disabled, Kessler, Pardue Lin and WSM6), boundary layer (YSU, MYJ, and BouLac) and surface layer schemes per case; (2) modified topography, which involved reducing mountains to 30% of their initial height; and (3) SST distributions for C1 case, which involved two representations in the model (from ECMWF and the MSG geostationary satellite).

The model was evaluated by using three different approaches: standard statistical parameters, spectral representation, and the moments in image analysis. The differences among these simulations showed that changes in the model setup significantly changed the flow, ABL structure and radar reflectivity patterns. The comprehensive analysis suggested the following:

- Several statistical parameters that were used for spatial and temporal in situ estimation generally substantiated the results of previous analyses for certain schemes: from a warm, dry and much deeper ABL with higher wind speeds in the nonlocal YSU scheme to a cold, moist and lower convective ABL and smaller wind speeds in the local MYJ scheme (e.g., Weisman et al. 2008; Kleczek et al. 2014; Milovac et al. 2016). The local BouLac scheme fell between these two extremes. The Kessler scheme often underestimated the wind and generally had worse scores (more so in C1 and less so in C2 and C3) than the more complex microphysics schemes (Pardue Lin and WSM6). However, both complex microphysics schemes were inferior selections as a model setup when combined with the YSU scheme. Although the selected microphysics highly influenced the temperature that was obtained by the MYJ

scheme, the results that were obtained from the local BouLac scheme exhibited minimal dependence. Among these simulations, the temporal estimation of the model [performed with both standard statistical measures and a spectral power distribution for in situ measurements (in Suppl. 1)] mostly confirmed the model's behavior in the spatial domain. The model underestimated the temperature (in all frequencies on a subdiurnal scale), although less so for the nonlocal YSU scheme and more so for the local ABL schemes. The energy from the humidity model was overestimated, particularly for MYJ combinations at a subdiurnal time scale.

- The moment invariant approach, showed the relevance of using radar reflectivity comparisons overcoming problems of in situ evaluations. This method revealed that the Kessler scheme (expectedly) provided relatively poor results and that the more complex microphysics schemes produced better matching. However, this matching depended on the chosen ABL scheme. Mature convection was somewhat underestimated in terms of the intensity, duration and coverage when using the YSU scheme, with a lack of stratiform cloudiness during the final stage. The opposite was observed for the local ABL schemes during the late afternoon hours, which showed overestimated convection with all the parameters. This observed overestimation was more pronounced in the MYJ than in BouLac schemes and using the WSM6 rather than Pardue Lin schemes. Although the method has certain limitation if the signal in the input image is a small one (unfavorable signal-to-noise relationship typical for very weak developed convection), the results here proved that the method offer a valuable additional information in model evaluating of convection (radar reflectivity) representing also a novelty of this study. Moreover, the ABL scheme was as least equally important as the chosen microphysics schemes for this study, which agrees with Cohen et al. (2015), who also stated the importance of good representations of lower-tropospheric structures (i.e., low-level lapse rate, vertical wind shear, buoyancy and mixed-layer CAPE) during severe weather conditions.
- The differences among the ABL schemes and SB characteristics were very consistent because of the differences in the HF, ABL heights and near-surface humidity. Different HF values were the primary reason for the different development and evolution of SBs: the greatest amount of HF (the driest ABL) in the YSU scheme created faster and more developed SBs (sometimes less realistic) than those in the MYJ and BouLac schemes. The heat (and moisture) fluxes were then transported throughout the ABL and interacted with the model's microphysics.

Although all the methods that were applied to these various parameters did not provide advantages over the same combinations of schemes, the results did not show very high sensitivity to the evaluation method that was used for verification. In this study, the MYJ_Lin experiments generally better matched the different verification fields. However, better matching can be also affected by the error compensations during the evaluation of the model setup.

Additional numerical tests revealed the influence of the topography on the SB–Cb characteristics. Reducing the mountains' heights decreased the HF, which affected the local flows. Instead of a slope-SB wind system, only SBs developed along the eastern area of the peninsula and the SBs in the Gulf of Trieste intensified, which consequently supplied the coastal region with more low-level moisture. In such circumstances, the penetration of the western SB was lower and occurred 1 h later, accompanied by somewhat lower speeds and lower heights of the SB body and SB front (in the Lin_MYJ_MT_C1 case and Lin_MYJ_MT_C2 case).

The HF and CIN values increased with higher terrain, contrary to the latent heat flux and CAPE values (in agreement with Barthlott and Kirshbaum 2013; Teixeira et al. 2014). Terrain modification showed that the unmodified mountain range influenced to the pre-thunderstorm characteristics: (1) higher mid-tropospheric moisture and HF values, (2) more strongly developed outflows, and their corresponding gust fronts on the leeward side. They consequently effected on the total convergence in the convergence zone, particularly for large-scale wind from northern directions, in terms of the

- timing (storms developed 1 h earlier);
- number of convective cells (increasing) and differences in their size (larger);

- intensity (stronger thunderstorms and relatively larger rain amounts); and
- locations of these thunderstorms.

Although the mountain range controlled the onset and accelerated the convection, the ABL convergence zone was still the main mechanism that fed existing and generated new daytime convective cells along the peninsula.

Although less visible from the statistical parameters, the model results showed certain improvements in terms of the convection's evolution, duration and intensity and in the lowermost coastal wind and humidity when using more realistic SST information in the model. The results also revealed that higher SST affected the SBs and, consequently, the convection in the Lin_MYJ_C1 run through (1) higher generated surface sensible HF values and (2) early-morning higher humidity values in the ABL and mid-level troposphere, which caused earlier, faster and shorter thunderstorm development. Higher SST fields (from ECMWF) were less accurate, which affected the other spatial fields and produced quantitatively less accurate convective activity and precipitation.

According to the first two points and the study by Miglietta et al. (2011), this SST–HF relationship should generate stronger convective activity in Lin_MYJ_C1 case. However, this earlier and faster convection produced a negative feedback on the further development of SBs, which were the main source of the low-level moisture supply. Therefore, in the Lin_MYJ_SST_C1 run, in which later and slower SB–Cb evolution occurred, the final results were somewhat stronger convergence, updrafts and convective activity itself. Therefore, the temporal relationship between the occurrence of SBs and Cbs is crucial to determine their life span. This result provides a new view of this (nonlinear) interaction.

Even the small changes in the SST field obviously have a further affect the characteristics and dynamics of SBs and convection. The accuracies of the modelled values of the 10-m horizontal velocity, 2-m temperature and rh showed that the results from the sensitivity test with variable SST always better matched the observations. This result can be a strong argument for the implementation of an hourly updated SST field in the model. Although this study presented only one study

case for a region in Croatia, this research still revealed some similarities to the results from other published studies (e.g., Miglietta et al. 2011; Tang 2012; Sweeney et al. 2014), and its conclusions suggest that the inclusion of a diurnal SST cycle in this model can be very important to produce more accurate weather forecasts.

Appendix 1

Modification of the Topography (Učka and Ćićarija Mountains)

The impact of the terrain height on the ("pure") SB characteristics (without convection) over Istria was already estimated in Prtenjak et al. (2006). In that study, one designed test had greatly idealized terrain height (h) over Istria and Kvarner Bay where h did not exceed 10 m asl. In such circumstances, the main convergence zone over peninsula had very unrealistic lifetime and position in space compared to the "real" case due to significant change in SBs evolutions. Here we wanted to examine only the influence of high mountains and the reduction to approximately 30% corresponds to leveling of mountains with other surrounding terrain without abrupt transitions (Fig. 14). Therefore, topography was modified by a
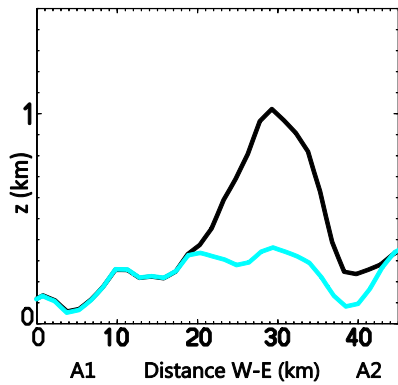
Figure 14

A comparison between initial (*black*) and modified (*blue*) topography over one arbitrary chosen vertical cross-section *A1A2* shown by *dashed line* in Fig. 1

simple cosine weight function (Eq. 1), which is zero at the boundary and one in the center, as defined over a 100×100 point square area; Fig. 1.

$$z(x,y) = \frac{(\cos(x \cdot \pi/50) + 1)(\cos(y \cdot \pi/50) + 1)}{4};$$
$$x,y \in [-50, 50] \qquad (1)$$

The cosine weights were then subtracted from 1 according to Eq. (2), producing weights that reduced the terrain height through simple multiplication. A "uniform" height reduction was achieved by raising the subtracted weights to the power of 100. Another sought effect was to avoid producing sharp gradients at the boundary, which would induce errors and instabilities during integration.

$$\text{filter}_{\text{original}}(x,y) = (1 - 0.1 \cdot z)^{100} \qquad (2)$$

The final weight function was then rescaled by Eq. (3) to have a value of 0.9 at its minimum, and 1 at its border.

$$\text{filter}_{\text{rescaled}}(x,y) = 0.9 + 0.1$$
$$\times \frac{(\text{filter}_{\text{original}} - \min(\text{filter}_{\text{original}}))}{(\max(\text{filter}_{\text{original}}) - \min(\text{filter}_{\text{original}}))}$$
$$(3)$$

The weight function that was used on the topography data was constructed by the former function and raised to the power of 12, which would reduce the height to approximately 30% around its center point (Fig. 14) according to:

$$\text{filter}_{30\%}(x,y) = (\text{filter}_{\text{rescaled}})^{12}. \qquad (4)$$

Appendix 2

Moment Invariants (IMA) Approach

The IMA approach is invariant to the translation, rotation and scale of the input image. The initial problem of inputting radar images is a spherically symmetrical issue that is why Zernike moments were chosen for analysis (Teague 1980). These are given as projections of an image function $f(x, y)$ on a unit circle:

$$A_{pq} = \frac{p+1}{\pi} \iint Z_{pq}(r, \theta) f(x,y) \mathrm{d}x \mathrm{d}y, \qquad (5)$$

where $x = r \cdot \cos \theta$ and $y = r \cdot \sin \theta$ and $Z_{pq}(r, \theta) = R_{pq}(r) e^{iq\theta}$ is the Zernike function of order $p + q$ in polar coordinates (r is a radial vector and θ is an angle with a positive x-axis) and

$$R_{pq}(r) = \sum_{k=0}^{(p-|q|)/2} \frac{(-1)^k (p-k)!}{k! \left(\frac{p+|q|}{2} - k\right)! \left(\frac{p-|q|}{2} - k\right)!} r^{p-2k} \qquad (6)$$

is the radial polynomial. The advantages of this approach are fast and relatively simple computation and a satisfactory signal-to-noise ratio (e.g., Wee and Paramesran 2007).

All the images that were used (e.g. Fig. 3 but without wind vectors) in this comparison were first represented as real-valued images of size 694×694 pixels with 256 gray scale levels (8-bit). The set of measured radar images was used as the reference set (Fig. 3). The procedure to obtain the measure of similarity between two images, namely, i from the model set and j from the referent set, was as follows:

(1) calculate of the first eight orders of Zernike moments by using Eq. (1) and (2) compare of each moment of the set that was calculated for image i with the corresponding moment of the reference image j by using the formula for Euclidean distance ED_{ij} between images i and j:

$$\mathrm{ED}_{ij} = \sum_{p,q=0}^{7} \left| (A_{pq})_i - (A_{pq})_j \right| \qquad (7)$$

A situation without any radar reflectivity (e.g., Fig. 2a), when only the shoreline contour was present on the input image, was considered a zero-order signal, and the corresponding ED_{ij} value was subtracted from all other values. Thus, the final ED_{ij} values showed similarity between the model results and the radar images.

REFERENCES

Acs, F., Gyöngyösi, A. Z., Breuer, H., Horváth, A., Mona, T., & Rajkai, K. (2014). Sensitivity of WRF-simulated planetary boundary layer height to land cover and soil changes. *Meteorologische Zeitschrift, 23,* 279–293.

Andrejczuk, M., Moszkowicz, S., Haman, K. E., & Szoplik, T. (2003). Radar-echo tracking by use of invariant moments. *Applied Optics, 42,* 5891–5896.

Arakawa, A., & Jung, J.-H. (2011). Multiscale modeling of the moist-convective atmosphere—A review. *Atmospheric Research, 102,* 263–285.

Babić, K., Mikuš, P., & Prtenjak, M. T. (2012). The relationship between shallow thermal circulation regimes and cumulonimbus clouds along the northeastern Adriatic coast. *Geofizika, 29,* 103–120.

Barthlott, C., & Kirshbaum, D. J. (2013). Sensitivity of deep convection to terrain forcing over Mediterranean islands. *Quarterly Journal of the Royal Meteorological Society, 139,* 1762–1779.

Beaver, S., Tanrikulu, S., Palazoglu, A., Singh, A., Soong, S. T., Jia, Y., et al. (2010). Pattern-based evaluation of coupled meteorological and air quality models. *Journal of Applied Meteorology and Climatology, 49,* 2077–2091.

Bellerby, T. J. (2004). A feature-based approach to satellite precipitation monitoring using geostationary IR imagery. *Journal of Hydrometeorology, 5,* 910–921.

Bougeault, P., & Lacarrère, P. (1989). Parameterization of orography-induced turbulence in a mesobeta-scale model. *Monthly Weather Review, 17,* 1872–1890.

Brooks, H. E., Lee, J. W., & Craven, J. P. (2003). The spatial distribution of severe thunderstorm and tornado environments from global reanalysis data. *Atmospheric Research, 67–68,* 73–94.

Challa, V. S., Indracanti, J., Rabarison, M. K., Patrick, C., Baham, J. M., Young, J., et al. (2009). A simulation study of mesoscale coastal circulations in Mississippi Gulf coast. *Atmospheric Research, 91,* 9–25.

Chen, S.-H., & Sun, W.-Y. (2002). A one-dimensional time-dependent cloud model. *Journal of the Meteorological Society of Japan, 80,* 99–118.

Clark, A. J., Gallus, W. A., Jr., & Weisman, M. L. (2010a). Neighborhood-based verification of precipitation forecasts from convection-allowing NCAR WRF model simulations and the operational NAM. *Weather and Forecasting, 25,* 1495–1509.

Clark, A. J., Gallus, W. A., Jr., Xue, M., & Kong, F. (2010b). Growth of spread in convection-allowing and convection-parameterizing ensembles. *Weather and Forecasting, 25,* 594–612.

Cohen, A. E., Cavallo, S. M., Coniglio, M. C., & Brooks, H. E. (2015). A review of planetary boundary layer parameterization schemes and their sensitivity in simulating southeastern U.S. cold season severe weather environments. *Journal of Applied Meteorology and Climatology, 30,* 591–612.

Crook, N. A. (1996). Sensitivity of moist convection forced by boundary layer processes to low-level thermodynamic fields. *Monthly Weather Review, 129,* 1550–1563.

Crook, N. A. (2001). Understanding Hector: The dynamics of island thunderstorms. *Monthly Weather Review, 124,* 1767–1785.

Crosman, E. T., & Horel, J. D. (2010). Sea and lake breezes: A review of numerical studies. *Boundary-Layer Meteorology, 137,* 1–29.

Demoli, N., Mrčela, I., & Šariri, K. (2013). Correlation and image moment approaches to analyze the Glagolitic script carved in stone tablets. *Optik, 124,* 1424–1430.

Dudhia, J. (1989). Numerical study of convection observed during the winter monsoon experiment using a mesoscale two-dimensional model. *Journal of the Atmospheric Sciences, 46,* 3077–3107.

Dudhia, J. (1996). A multi-layer soil temperature model for MM5. *The Sixth PSU/NCAR Mesoscale Model Users' Workshop*, pp. 22–24.

Feudale, L., & Manzato, A. (2014). Cloud-to-ground lightning distribution and its relationship with orography and anthropogenic emissions in the Po Valley. *Journal of Applied Meteorology and Climatology, 53,* 2651–2670.

Feudale, L., Manzato, A., & Micheletti, S. (2013). A cloud-to-ground lightning climatology for north-eastern Italy. *Advances in Science and Research, 10,* 77–84.

Franchito, S. H., Rao, V. B., Stech, J. L., & Lorenzzetti, J. A. (1998). The effect of coastal upwelling on the sea-breeze circulation at Cabo Frio, Brazil: A numerical experiment. *Annales Geophysicae, 16,* 866–881.

Franchito, S. H., Toda, T. O., Rao, V. B., & Kayano, M. T. (2008). Interaction between coastal upwelling and local winds at Cabo Frio, Brazil: An observational study. *Journal of Applied Meteorology and Climatology, 47,* 1590–1598.

Gilland, E. K., & Rowe, C. M. (2012). A comparison of cumulus parameterization schemes in the WRF model. 2012 AMS annual meeting, P2.16. https://ams.confex.com/ams/pdfpapers/120591.pdf. Accessed December 2, 2016.

Givati, A., Lynn, B., Liu, Y., & Rimmer, A. (2012). Using the WRF model in an operational stream forecast system for the Jordan River. *Journal of Applied Meteorology and Climatology, 51,* 285–299.

Gómez-Navarro, J. J., Raible, C. C., & Dierer, S. (2015). Sensitivity of the WRF model to PBL parametrisations and nesting techniques: Evaluation of wind storms over complex terrain. *Geoscientific Model Development, 8,* 3349–3363.

Güttler, I., Stepanov, I., Branković, Č., Nikulin, G., & Jones, C. (2015). Impact of horizontal resolution on precipitation in complex orography simulated by the regional climate model RCA3. *Monthly Weather Review, 143,* 3610–3627.

Hong, S. Y., & Lim, J. O. (2006). The WRF single-moment 6-class microphysics scheme (WSM6). *Journal of the Korean Meteorological Society, 42,* 129–151.

Hong, S. Y., Noh, Y., & Dudhia, J. (2006). A new vertical diffusion package with an explicit treatment of entrainment processes. *Monthly Weather Review, 134,* 2318–2341.

Horvath, K., & Vilibić, I. (2014). Atmospheric mesoscale conditions during the Boothbay meteotsunami: a numerical sensitivity study using a high-resolution mesoscale model. *Natural Hazards, 74,* 55–74.

Janjić, Z. I. (1994). The step-mountain eta coordinate model: Further developments of the convection, viscous sublayer, and turbulence closure schemes. *Monthly Weather Review, 122,* 927–945.

Jury, M. R., & Chiao, S. (2013). Leeside boundary layer confluence and afternoon thunderstorms over Mayaguez, Puerto Rico. *Journal of Applied Meteorology and Climatology, 52,* 439–454.

Kessler, E. (1995). On the continuity and distribution of water substance in atmospheric circulations. *Atmospheric Research, 38,* 109–145.

Kleczek, M. A., Steeneveld, G.-J., & Holtslag, A. A. M. (2014). Evaluation of the weather research and forecasting mesoscale model for GABLS3: Impact of boundary-layer schemes, boundary conditions and spin-up. *Boundary-Layer Meteorology, 152,* 213–243.

Lin, Y.-L., Richard, D. F., & Harold, D. O. (1983). Bulk parameterization of the snow field in a cloud model. *Journal of Applied Meteorology and Climatology, 22,* 1065–1092.

Mayor, Y. G., & Mesquita, M. D. S. (2015). Numerical simulations of the 1 May 2012 deep convection event over Cuba: Sensitivity to cumulus and microphysical schemes in a high-resolution model. *Advances in Meteorology, 2015.* doi:10.1155/2015/973151.

Menendez, M., Garcia-Diez, M., Fita, L., Fernandez, J., Mendez, F. J., & Gutierrez, F. J. (2014). High-resolution sea wind hindcasts over the Mediterranean area. *Climate Dynamics, 42,* 1857–1872.

Meteorological Office. (1962). *Weather in the Mediterranean* (Vol. 1). London: General Meteorology, Her Majesty's Stationery Office.

Miao, J. F., Wyser, K., Chen, D., & Ritchie, H. (2009). Impacts of boundary layer turbulence and land surface process parameterizations on simulated sea breeze characteristics. *Annales Geophysicae, 27,* 2303–2320.

Miglietta, M. M., Moscatello, A., Conte, D., Mannarini, G., Lacorata, G., & Rotunno, R. (2011). Numerical analysis of a Mediterranean 'Hurricane' over south-eastern Italy: Sensitivity experiments to sea surface temperature. *Atmospheric Research, 101,* 412–426.

Mikuš, P., Prtenjak, M. T., & Strelec-Mahović, N. (2012). Analysis of the convective activity and its synoptic background over Croatia. *Atmospheric Research, 104–105,* 139–153.

Milovac, J., Warrach-Sagi, K., Behrendt, A., Späth, F., Ingwersen, J., & Wulfmeyer, V. (2016). Investigation of PBL schemes combining the WRF model simulations with scanning water vapor differential absorption lidar measurements. *Journal of Geophysical Research*, *121*, 624–649 (2016). doi:10.1002/2015JD023927.

Mlawer, E. J., Taubmanm, S. J., Brown, P. D., Iacono, M. J., & Clough, S. A. (1997). Radiative transfer for inhomogeneous atmospheres: RRTM, a validated correlated-k model for the longwave. *Journal of Geophysical Research, 102,* 16663–16682.

Mohan, M., & Bhati S., (2011). Analysis of WRF model performance over subtropical region of Delhi, India. *Advances in Meteorology, 2011.* doi:10.1155/2011/621235.

Penzar, B., Penzar, I., & Orlić, M. (2001). *Vrijeme i klima hrvatskog Jadrana.* Zagreb: Nakladna kuća Dr. Feletar.

Petrova, S., Mitzeva, R., & Kotroni, V. (2014). Summer-time lightning activity and its relation with precipitation: Diurnal variation over maritime, coastal and continental areas. *Atmospheric Research, 135–136,* 388–396.

Pielke, R. A. (2002). *Mesoscale meteorological modeling.* New York: Academic Press.

Poljak, G., Prtenjak, M. T., Kvakić, M., Strelec-Mahović, N., & Babić, K. (2014). Wind patterns associated with the development of daytime thunderstorms over Istria. *Annales Geophysicae, 32,* 401–420.

Prein, A. F., Gobiet, A., Truhetz, H., Keuler, K., Goergen, K., Teichmann, C., et al. (2016). Precipitation in the EURO-CORDEX 0.11° and 0.44° simulations: High resolution, high benefits? *Climate Dynamics, 46,* 383–412.

Prtenjak, M. T. (2003). Main characteristics of sea/land breezes along the eastern coast of the northern Adriatic. *Geofizika, 20,* 75–92.

Prtenjak, M. T., Grisogono, B., & Nitis, T. (2006). Shallow mesoscale flows at the north-eastern Adriatic coast. *Quarterly Journal of the Royal Meteorological Society, 132,* 2191–2216.

Prtenjak, M. T., Horvat, I., Tomažić, I., Kvakić, M., Viher, M., & Grisogono, B. (2015). Impact of mesoscale meteorological processes on anomalous radar propagation conditions over the northern Adriatic area. *Journal of Geophysical Research, 120,* 8759–8782.

Prtenjak, M. T., Pasarić, Z., Orlić, M., & Grisogono, B. (2008). Rotation of sea/land breezes along the northeastern Adriatic coast. *Annales Geophysicae, 26,* 1711–1724.

Segal, M., & Pielke, R. A. (1985). On the effect of water temperature and synoptic flows on the development of surface flows over narrow elongated water bodies. *Journal of Geophysical Research, 90,* 4907–4910.

Skamarock, W. C., & Klemp, J. B. (2008). A time-split nonhydrostatic atmospheric model for weather research and forecasting applications. *Journal of Computational Physics, 227,* 3465–3485.

Skamarock, W. C., Klemp, J. B., Dudhia, J., Gill, D. O., Barker, D. M., Duda, M. G., et al. (2008). *A description of the advanced research WRF version 3, NCAR/TN-475+STR.* Boulder: NCAR.

Sović, I., Šariri, K., & Živčić, M. (2013). High frequency microseismic noise as possible earthquake precursor. *Research in Geophysics, 3,* 8–12.

Stanešić, A., & Brewster, K. A. (2015). Impact of radar data assimilation on the numerical simulation of a severe storm in Croatia. *Meteorologische Zeitschrift, 25,* 37–53.

Sweeney, J. K., Chagnon, J. M., & Gray, S. L. (2014). A case study of sea breeze blocking regulated by sea surface temperature along the English south coast. *Atmospheric Chemistry and Physics, 14,* 4409–4418.

Tang, Y. (2012). The effect of variable sea surface temperature on forecasting sea fog and sea breezes: A case study. *Journal of the Atmospheric Sciences, 51*(986–990), 2012.

Teague, M. R. (1980). Image analysis via the general theory of moments. *Journal of the Optical Society of America, 70,* 920–930.

Teixeira, J. C., Carvalho, A. C., Carvalho, M. J., Luna, T., & Rocha, A. (2014). Sensitivity of the WRF model to the lower boundary in an extreme precipitation event—Madeira island case study. *Natural Hazards and Earth System Sciences, 14,* 2009–2025.

Thunis, P., & Bornstein, R. (1996). Hierarchy of mesoscale flow assumptions and equations. *Journal of the Atmospheric Sciences, 53,* 380–397.

van Delden, A. (2001). The synoptic setting of thunderstorms in western Europe. *Atmospheric Research, 56,* 89–110.

Večenaj, Ž., Belušić, D., Grubišić, V., & Grisogono, B. (2012). Along-coast features of the bora related turbulence. *Boundary-Layer Meteorology, 143,* 527–545.

Wang, D., Miao, J., & Tan, Z. (2013). Impacts of topography and land cover change on thunderstorm over the Huangshan (Yellow Mountain) area of China. *Natural Hazards, 67,* 675–699.

Wee, C.-Y., & Paramesran, R. (2007). On the computational aspects of Zernike moments. *Image and Vision Computing, 25,* 967–980.

Weisman, M. L., Christopher, D., Wang, W., Manning, K. W., & Klemp, J. B. (2008). Experiences with 0–36-h explicit convective forecasts with the WRF-ARW model. *Weather and Forecasting, 23,* 407–437.

Žabkar, R., Koračin, D., & Rakovec, J. (2013). A WRF/Chem sensitivity study using ensemble modelling for a high ozone episode in Slovenia and the northern Adriatic area. *Atmospheric Environment, 77,* 990–1004.